Politecnico di Torino

Master's Degree in Mechanical Engineering

Academic Year 2024/2025

October 2025

Design, prototyping and testing of an accelerometer for space missions

Supervisors:

Prof. Angelo Lerro

Prof. Eleonora Atzeni

Ph.D Marco Pisani

Candidate:

Alessandro Bolognini

Abstract

The growing demand for precise and accurate measurement systems in space missions has stimulated the development of innovative solutions in the field of accelerometers, capable of delivering high sensitivity and low noise measurement over a wide frequency range. To achieve these requirements, an accelerometer based on a mass–spring system with a low natural frequency is needed, since both acceleration noise and sensitivity are related to the square of the natural frequency. This thesis addresses this challenge through the design, prototyping, and testing of an elastic suspension for a new accelerometer architecture intended for space applications, employing a heterodyne laser interferometry readout to detect the displacements of the proof mass. The research also encompasses the development of a dedicated test bench for the qualification of the accelerometer under microgravity conditions and the optimization of the data acquisition software. Based on the assessment of the technological framework and the defined system requirements—specifically, the need for the first natural frequency to be below 1 Hz—a prototype was developed, consisting of a beryllium–copper alloy proof mass and a titanium alloy spring manufactured using Powder Bed Fusion–Laser Beam, an additive manufacturing technique. The prototyping of the elastic suspension was complemented by laboratory experimental tests and the validation of finite element models. The test bench was equipped with an optical acquisition system controlled via LabVIEW software, together with video monitoring and additional sensors managed by microcontrollers. The analysis of the results obtained on the spring confirmed that the required specifications were satisfied.

Contents

List of Figures

List of Tables

Introduction

This thesis continues a research project previously initiated under the title *"Design of the Elastic Suspension for a New Concept Accelerometer for Space Applications: LIG-ACUBE Mission"* [1]. It brings together both numerical and experimental activities: while the numerical analysis is mainly devoted to verifying and validating the developed physical model, the central focus lies on the experimental design and implementation of the system.

The work was conducted at the Istituto Nazionale di Ricerca Metrologica (INRiM), in collaboration with the Interdepartmental Center of Integrated Additive Manufacturing (IAM@PoliTO) of Politecnico di Torino. The main objective is the design and prototyping of an elastic suspension for an accelerometer intended for space applications, together with the development of a dedicated test bench for performance validation under microgravity conditions.

The accelerometer readout is based on a laser interferometric measurement principle, a technique that offers very high sensitivity and low noise. Interferometry has already proven its value in space missions: in GRACE-FO it was used to track the relative distance between twin satellites, while in LISA Pathfinder it allowed the monitoring of the motion of free-falling test masses with resolutions of 32 fm/$\sqrt{\text{Hz}}$. These examples highlight the competitiveness of interferometric methods in terms of metrological performance.

The activities described in this thesis represent an essential step toward the functional validation and preliminary qualification of the prototype, thereby creating the conditions for its potential integration in future space missions, such as the LIG-A Cube project proposed by the European Space Agency (ESA).

The structure of the thesis reflects the progression of the project: it begins with

a review of the state of the art in space accelerometry, the LIG-A Cube mission, and experimental approaches to microgravity. It then outlines the previous research while the following chapters detail the design and prototyping of the elastic suspension, the construction of the microgravity test bench, and the validation of the proposed solution.

Finally, an appendix provides technical information on the experimental facility employed for the zero-gravity tests.

State of the Art

1.1 Accelerometers for Space Applications

An accelerometer is a device that determines the acceleration of a test mass with respect to the structure to which it is attached. An accelerometer operates by detecting the reactive force acting on its proof mass whenever the system experiences non-inertial motion. In essence, the device measures deviations from an ideal inertial trajectory, making it sensitive to both gravitational and non-gravitational forces that induce acceleration. In satellites, for example, it detects departures from free fall by observing the relative motion between the mass and the surrounding frame.

Since the measurement is always referenced to the body on which the accelerometer is installed, the sensor output depends on the local environment. For instance, a unit fixed on a stationary platform on Earth with a vertical sensing axis would produce a constant signal of approximately $g = 9.81\,\mathrm{m/s^2}$. This steady output does not indicate movement but represents the effect of the gravity oh Earth on the test mass. This behavior will be analyzed in Chapter 4, during the experimental characterization of the MEMS accelerometer.

Accelerometers are widely employed in space applications, from monitoring tasks to primary scientific measurements. On the International Space Station (ISS), they track microgravity conditions inside different modules, whereas in missions dedicated to geodesy or fundamental physics they must operate with extremely high sensitivity, particularly at very low frequencies, down to 10^{-3}–$10^{-4}\,\mathrm{Hz}$.

The signals recorded inside a spacecraft combine contributions from gravitational

and non-gravitational effects. The first are caused by celestial bodies or local mass distributions, while the second include atmospheric drag, solar radiation pressure, and internal disturbances such as thermal gradients or pressure fluctuations. In drag-free satellites, the accelerometer reading is used to command micro-thrusters that cancel the non-gravitational forces, allowing the spacecraft to follow the free-fall motion of the test mass and experience only gravity.

Finally, it should be emphasized that the instrument simply measures the total acceleration acting on the mass, without distinguishing the physical origin of the forces. For this reason, accelerometers are sometimes described as "inertial sensors," although the term can be misleading in the presence of local perturbations. To extract meaningful information, the measurements require careful modeling and post-processing to separate the useful signal from background noise and spurious effects.

1.2 Capacitive Accelerometers

Capacitive accelerometers represent the most widely adopted technology for high-precision space missions. Among them, two architectures stand out: electrostatic accelerometers such as the ones developed by ONERA (France), and the ISA (Italian Spring Accelerometer), which features mechanical suspension. Both designs rely on capacitive readout for position sensing, but they differ significantly in their suspension methods and system stability.

1.2.1 Electrostatic Accelerometers

Electrostatic accelerometers, such as those designed by ONERA, are based on a test mass electrostatically suspended between capacitor plates. This architecture was adopted in landmark missions including CHAMP, GOCE, GRACE, GRACE-FO, and MICROSCOPE. The mass is kept near the center of the cavity by actively applying electrostatic forces, which are controlled in real-time according to position signals derived from capacitive sensing.

A key challenge of this configuration is its intrinsic instability: the electrostatic force exhibits negative stiffness, causing the test mass to be naturally attracted to the nearest electrode.

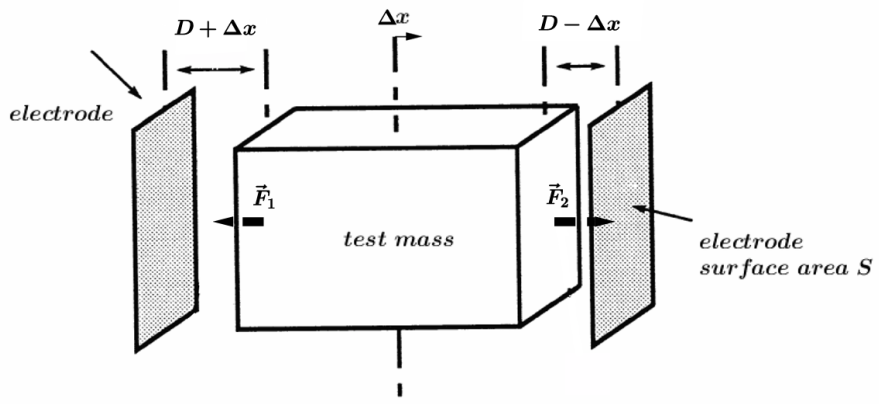

Figure 1.1: Working principle of an electrostatic accelerometer [2].

The ONERA electrostatic accelerometer operates by suspending a test mass between capacitor plates, using electrostatic attraction to maintain it near the center of the cavity. A potential difference V applied between the electrodes and the mass generates an electrostatic force that increases nonlinearly as the mass moves closer to either electrode. The control system relies on a feedback loop to apply a restoring force that keeps the mass centered.

Assuming parallel plate geometry (Figure 1.1), the electrostatic force acting along the sensitive axis x is given by:

$$F_{\text{el}} = \frac{1}{2} \cdot \frac{\varepsilon_0 \cdot S \cdot V^2}{(D \pm \Delta x)^2} \tag{1.1}$$

where:

- ε_0: vacuum permittivity,
- S: surface area of the electrodes,
- D: nominal gap between the mass and each electrode,
- Δx: displacement from the central position.

Differentiating with respect to Δx yields the effective stiffness:

$$k_{\text{electrostatic}} = \frac{dF_{\text{el}}}{d\Delta x} \approx -\frac{2 \cdot \varepsilon_0 \cdot S \cdot V^2}{D^3} \tag{1.2}$$

The negative sign indicates an unstable equilibrium, requiring active control to counteract the attractive force and prevent the test mass from collapsing onto the electrodes.

The position of the test mass is measured by monitoring the variation in capacitance. The capacitance between the mass and each electrode is expressed as:

$$C = \frac{\varepsilon_0 \cdot S}{D \pm \Delta x} \tag{1.3}$$

For small displacements ($\Delta x \ll D$), the relative variation can be linearized:

$$\frac{\Delta C}{C} \approx -\frac{\Delta x}{D} \tag{1.4}$$

This relationship enables the reconstruction of the displacement and, by calibration, the estimation of the acceleration acting on the test mass.

To ensure adequate control authority, the gap D must be small—typically 300 to 600 μm; Figure 1.2 shows noise spectrum of the capacitance position sensor with 300 μm gap. However, such small separations amplify the influence of disturbances such as patch effects (local surface charge variations), residual gas damping, and electrostatic back-action. These phenomena limit the performance, particularly at low frequencies, where sensitivity is most critical for missions like MICROSCOPE.

An additional challenge arises from the accumulation of electric charge on the test mass due to cosmic rays. Charge is discharged via a thin gold wire connected to the structure, but the wire introduces thermal noise—especially at its bonding points—unless constructed using low-loss suspension techniques. Despite advancements such as the increased gap in the MICROSCOPE accelerometer, low-frequency noise remains a fundamental limitation in this class of instruments.

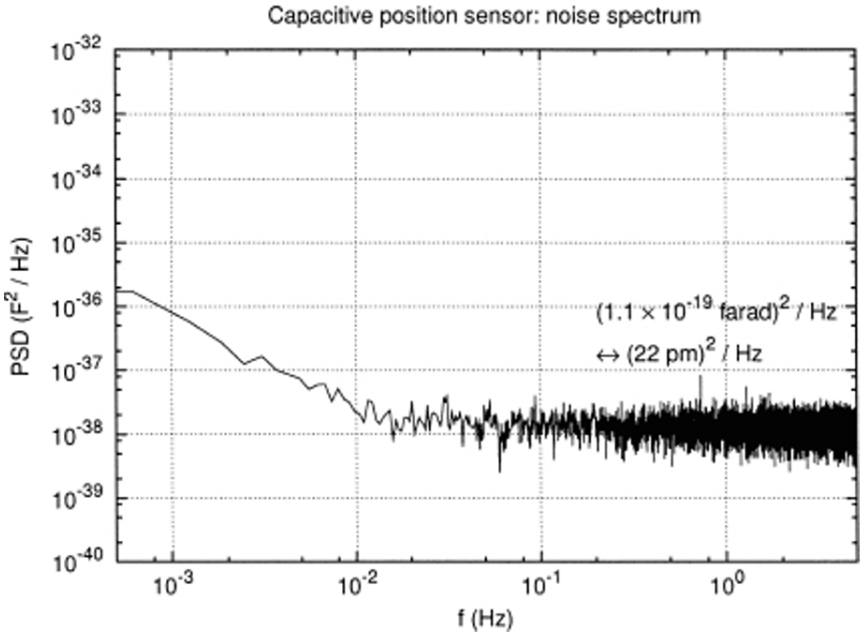

Figure 1.2: Noise spectrum of the capacitance position sensor by ONERA, with 300 µm gap [2].

1.2.2 ISA Accelerometer

The ISA (Italian Spring Accelerometer), currently onboard the ESA–JAXA *Bepi-Colombo* mission, adopts a distinct architecture based on mechanical suspension. The test mass is suspended by thin metallic flexures (lamellae) that provide both mechanical stiffness and electrical grounding. Unlike electrostatic suspension, the mechanical configuration ensures a positive stiffness and inherently stable equilibrium, eliminating the need for active control to maintain centering.

Position sensing is still performed capacitively, meaning that challenges such as small electrode gaps and low-frequency electronic noise persist. Nevertheless, the mechanical suspension mitigates some limitations found in electrostatic systems, notably the instability caused by negative stiffness and the influence of surface charge patches.

One limitation of the ISA configuration lies in its single-axis sensitivity: each

unit responds to accelerations along only one degree of freedom. For full three-dimensional measurements, three ISA units are mounted orthogonally, as shown in Figure 1.3a. While this increases system complexity and mass, it provides modularity and robustness. ISA accelerometers have also been deployed in marine geophysics, confirming their versatility across application domains.

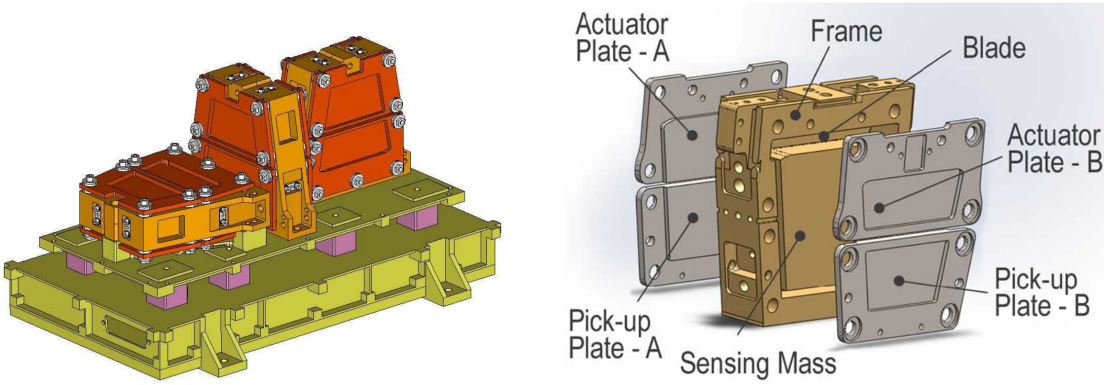

a) b)

Figure 1.3: a) Core of ISA detector assembly [3]; b) ISA, high sensitivity accelerometer [4].

BepiColombo, launched on October 20, 2018, is a joint ESA–JAXA mission dedicated to the comprehensive study of Mercury [5]. The spacecraft consists of two scientific modules: the Mercury Planetary Orbiter (MPO) and the Mercury Magnetospheric Orbiter (MIO).

The main science objectives of the mission include:

- Characterizing the internal structure of Mercury , including the size and physical state of its metallic core;
- Investigating the planet surface morphology, composition, and geological evolution;
- Studying the exosphere and magnetosphere and their interactions with the solar wind;

- Measuring the gravity field and rotational state of the planet;
- Testing general relativity through precision orbit tracking.

The interplanetary trajectory of the mission features multiple gravity-assist flybys (Earth, Venus, and Mercury) to achieve orbital insertion with minimal propellant use. Arrival at Mercury is scheduled for late 2025 or early 2026, depending on final cruise-phase adjustments. Scientific operations will begin after the MPO and MIO modules separate and transition into their respective orbital configurations.

ISA contributes to the Mercury Orbiter Radio-science Experiment (MORE), enabling precise measurement of non-gravitational perturbations such as solar radiation pressure. This data is essential for reconstructing the gravity field of Mercury and testing relativistic effects with unprecedented precision.

1.3 LIG-A CUBE SPACE MISSION

The *LIG-A CUBE* space mission, proposed by INRiM to the ESA, has the primary objective of demonstrating the performance of the *LIG-A* accelerometer (Laser Interferometry Gauge & Accelerometer). This instrument differs from other types of accelerometers used in space applications due to its measurement principle, which is based on a heterodyne laser interferometer.

This technique makes it possible to reduce the noise typically affecting high-sensitivity capacitive accelerometers, mainly caused by electrical noise resulting from the extremely small gaps required to achieve high sensitivity.

For the mission, a 20U CubeSat will be employed, where one unit (1U) corresponds to a volume of $10 \times 10 \times 10$ cm^3.

Of the total volume, 8U will be dedicated to the service platform, while the remaining 12U will be allocated to the payload, primarily consisting of the LIG-A accelerometers for the mission objectives. The satellite will be placed into a low Earth polar orbit, operating with a passive attitude control system oriented towards the Earth.

As previously introduced, the measurement system is based on a heterodyne laser interferometer. This technique relies on the use of two laser beams with slightly different frequencies. When the two beams are superimposed, they generate an interference signal at the beat frequency, called heterodyne frequency, corresponding to the frequency difference between the two sources:

$$f_b = \nu_2 - \nu_1$$

where ν_1 and ν_2 are the optical frequencies of the two laser beams.

If one of the beams is reflected by a moving target, the change in optical path length produces a phase shift in the beat signal, directly proportional to the displace-

ment. By measuring this phase variation, it is possible to determine the movement of the target with very high accuracy. This makes heterodyne interferometry a reliable, linear, and highly sensitive and precise technique, well suited for applications where precision is essential.

The interferometer employed in the mission is a miniaturized version of the instrument already developed at INRiM, known as LIG (Laser Interferometry Gauge). Figure 1.4 presents a schematic of the LIG system, which is composed of three main units:

- the Optoelectronic Board, hosting the instrumentation,
- the Optical Head, containing the optical components,
- the Electronics, responsable for the measurement of the phase shift.

In the figure, yellow lines indicate optical fibers, red lines represent the optical laser path, and blue lines correspond to the electrical connections.

The laser source of the LIG is a continuous-wave, high-performance planar waveguide external cavity laser (PW-ECL), specifically the model developed by Redfern Integrated Optics (RIO), operating at a wavelength of 1064 nm [6], which is the standard laser frequency for space applications also used in LISA Pathfinder [7] and GRACE Follow-On [8]. The laser beam is then split into two frequency components using acousto-optic modulators (AOMs).

Subsequently, through a combination of optical components, including beam splitters and polarizing beam splitters, the two beams are directed towards mirrors M_1 and M_2. Here, M_1 serves as the reference mirror, it will be fixed to the cage of the accelerometer, while M_2 will be fixed to the mass of the accelerometer. The beams are then detected by photodetectors, where the phase difference is processed electronically, enabling the precise determination of the target displacement.

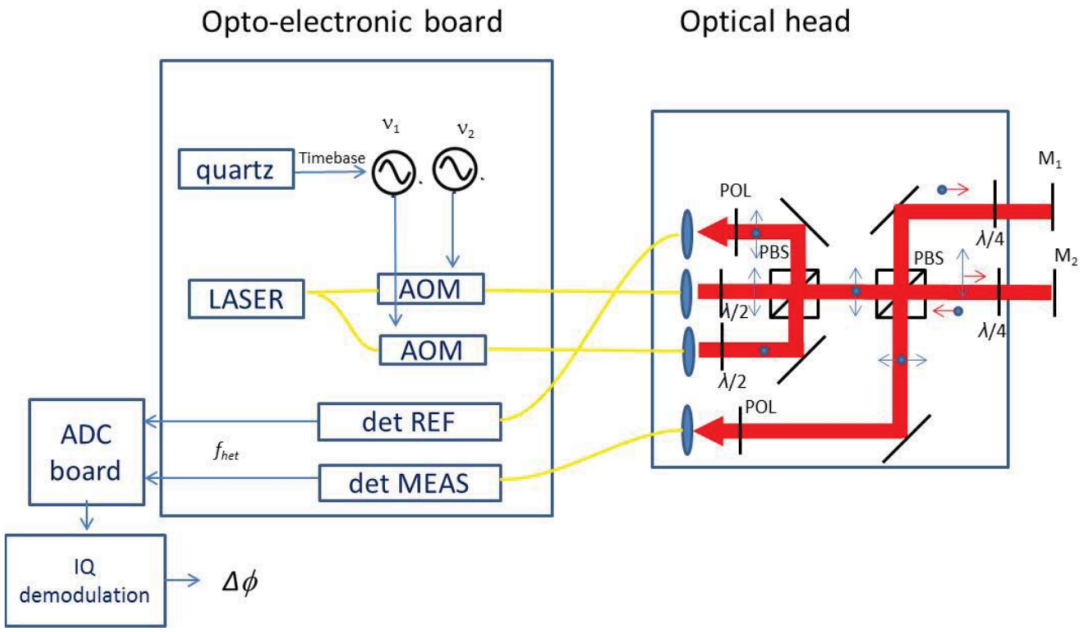

Figure 1.4: Schematic of the LIG [6].

Figure 1.5 shows the final setup of the LIG interferometer, realized in a quasi-monolithic layout, where the optical components are glued onto a Zerodur® base. The optical set-up is enclosed in a series of enclosures in order to mitigate the effect of environmental vibrations and temperature fluctuations.

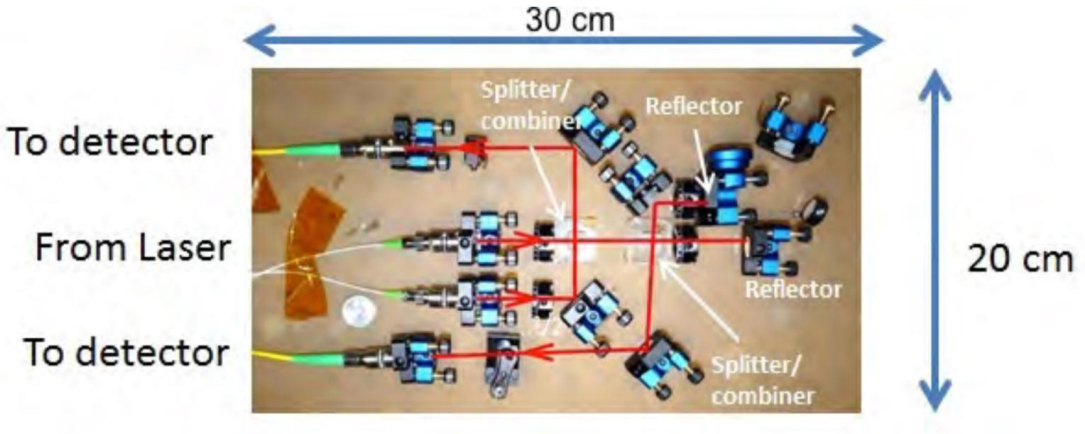

Figure 1.5: Picture of optical head of LIG [9].

To demonstrate the superior performance of the LIG, comparative tests were

carried out on an ISA-GGG accelerometer, which is equipped with a single-degree-of-freedom test mass and capacitive readout. For the experiment, an additional interferometric readout was implemented using the LIG system, by placing corner-cube reflectors on the moving mass. The two readouts, capacitive and interferometric, were acquired simultaneously, allowing for a direct real-time comparison of the same data — an approach never performed before [2].

Figure 1.6 reports the results of these measurements, in particular the spectral density of the displacement noise from both the capacitive sensor and the LIG interferometer. As can be seen, below 2 mHz the noise increases significantly due to local vibrations, a feature that affects both readouts equally. However, above 3 mHz the displacement noise measured with the LIG is approximately 40 times lower than that of the capacitive readout, clearly demonstrating its superior performance. The figure also shows a peak at 5.8 Hz in both measurements, corresponding to the first natural frequency, and another at 12 Hz, corresponding to the second natural frequency of the ISA accelerometer. Nevertheless, an unexplained peak slightly above 1 Hz appears in the interferometric readout [2].

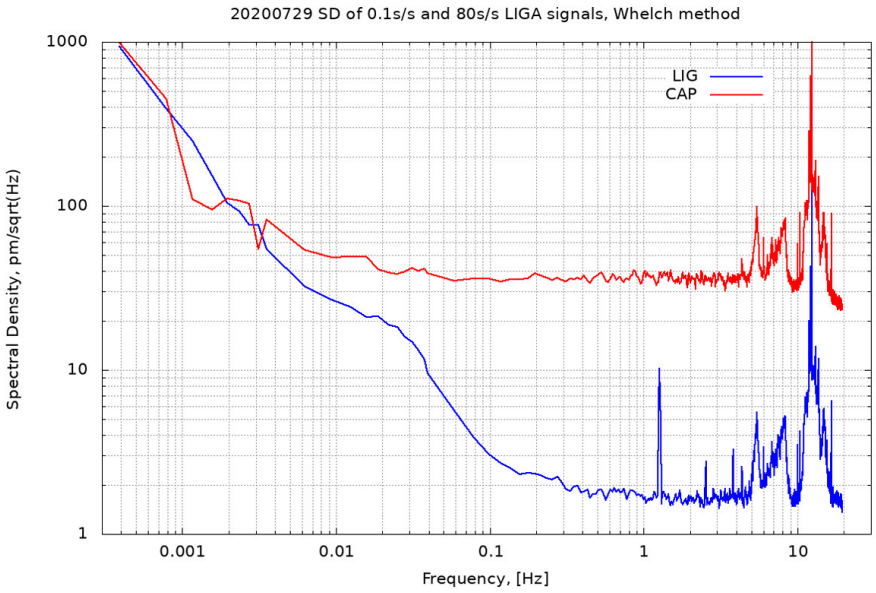

Figure 1.6: Spectral density of the capacitance (red) and LIG (blue) readout when interfaced to the same test mass [2].

Figure 1.7 shows the spectral density of the LIG displacement noise, measured in the frequency range from 10^{-5} Hz up to approximately 0.5 Hz, by placing the retro-reflectors on stable supports and removing the test mass. In this configuration, the noise level was reduced by about a factor of 3 at 0.1 Hz and by about a factor of 30 at 1 mHz. This improvement is most likely due to the fact that, with the test mass in place, the system was not perfectly constrained, thereby introducing additional noise contributions [2].

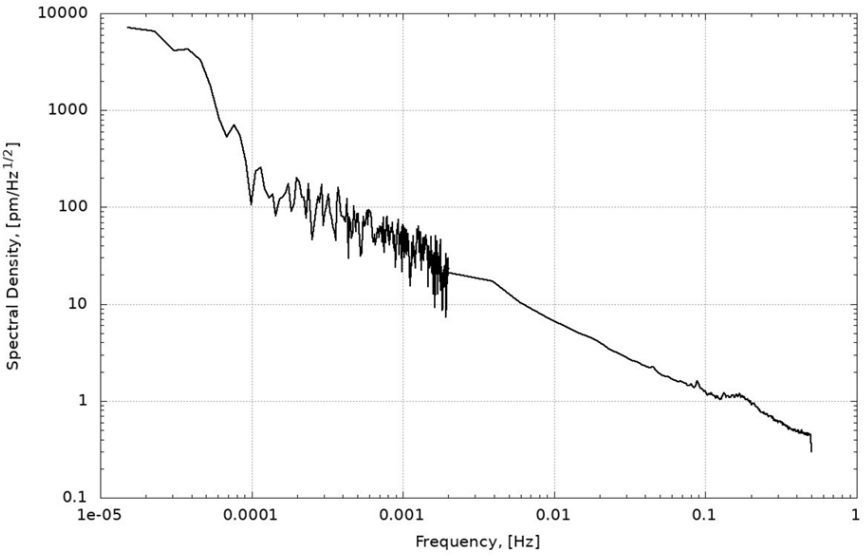

Figure 1.7: Spectral density of displacement noise of the LIG readout [2].

Our interest is the acceleration noise, which can be directly obtained from the displacement noise, since it is proportional to the square of the natural frequency. Indeed, the equation of motion of a mass–spring–damper system is a linear second-order differential equation with constant coefficients:

$$m\,\ddot{x} + c\,\dot{x} + k\,x = m\,a$$

where x is the relative displacement between the mass and the base, and a is the base acceleration.

The relation:

$$a \;\approx\; \omega_n^2\,x$$

holds in steady state for excitation frequencies below the system natural frequency ($\omega \ll \omega_n$), that is, when the relative displacement x is used to estimate the base acceleration.

The ISA-GGG natural frequency is $f_n = 5.8$ Hz, which corresponds to $\omega_n \approx$

$36.44\ \mathrm{rad\,s^{-1}}$ [2] .

From Figure 1.7, the displacement noise at 1 mHz is approximately $x \simeq 30\ \mathrm{pm}/\sqrt{\mathrm{Hz}} = 3.0 \times 10^{-11}\ \mathrm{m}/\sqrt{\mathrm{Hz}}$. Thus, the equivalent acceleration noise is

$$a(1\ \mathrm{mHz}) \approx \omega_n^2\, x = (36.44)^2 \times 3.0 \times 10^{-11} \approx 3.98 \times 10^{-8}\ \frac{\mathrm{m}}{\mathrm{s}^2\sqrt{\mathrm{Hz}}}.$$

Although the plot in Figure 1.7 does not extend up to 1 Hz, the measured displacement noise at this frequency does not exceed $0.35\ \mathrm{pm}/\sqrt{\mathrm{Hz}} = 3.5{\times}10^{-13}\ \mathrm{m}/\sqrt{\mathrm{Hz}}$. Therefore, the corresponding acceleration noise is

$$a(1\ \mathrm{Hz}) \approx \omega_n^2\, x = (36.44)^2 \times 3.5 \times 10^{-13} \approx 4.6 \times 10^{-10}\ \frac{\mathrm{m}}{\mathrm{s}^2\sqrt{\mathrm{Hz}}}.$$

In the LIG-A proposal submitted to ESA [2], the project objectives were explicitly defined as follows:

> *"The baseline LIG-A accelerometer shall demonstrate sensitivity across a broad frequency range, covering three decades from* 10^{-3} *Hz to* 1 *Hz. The target acceleration noise performance is* $5 \times 10^{-8}\ m/s^2/\sqrt{Hz}$ *at* 10^{-3} *Hz, decreasing to* $5{\times}10^{-10}\ m/s^2/\sqrt{Hz}$ *at* 1 *Hz. The realization will be limited to one degree of freedom (1D)."*

Thus, the stated goals have been successfully achieved in both cases.

In the LIG-A CUBE space mission, it was required to measure two degrees of freedom: one translational and one rotational. To achieve this, the payload will host two LIG-A interferometers, since each interferometer can measure only a single degree of freedom. For this reason, an evolution of the original LIG-A interferometric system has been developed specifically for this mission, in which two interferometers are integrated and miniaturized as much as possible, making this measurement approach suitable for a wider range of space applications. Consequently, two independent mass–spring systems are foreseen.

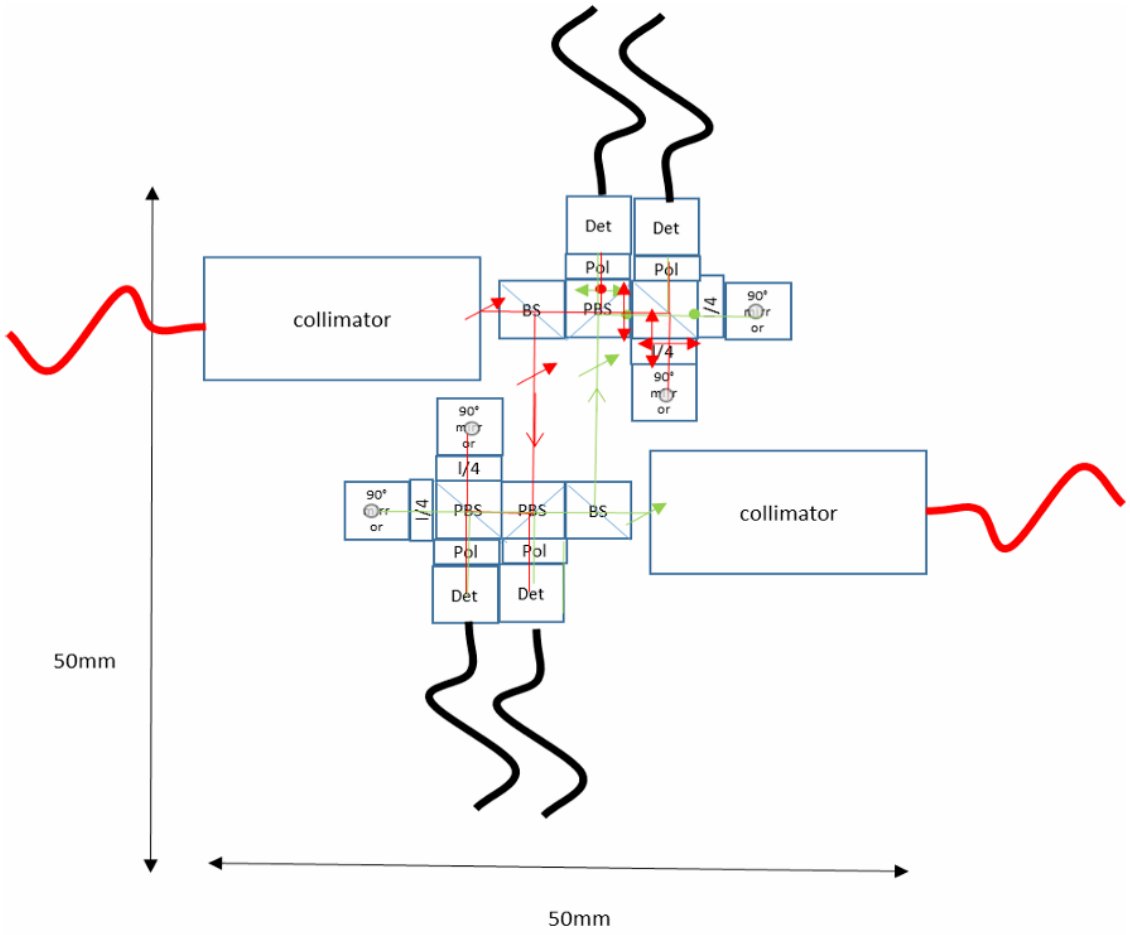

Figure 1.8: Schematic of the evolved LIG-A optical layout, front view [10].

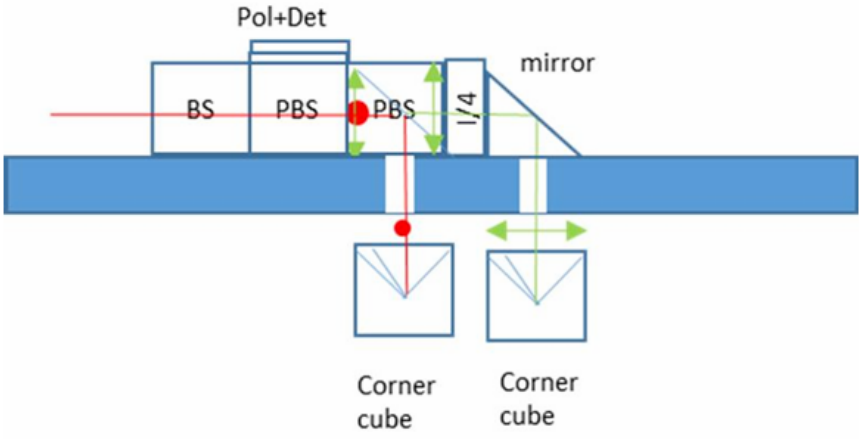

Figure 1.9: Schematic of the evolved LIG-A optical layout, side view [10].

Figure 1.8 shows the optical layout of this miniaturized evolution of the LIG-A,

where two interferometers are dedicated to the required degrees of freedom, while Figure 1.10 shows the actual configuration. The interferometers are assembled to maximize symmetry and minimize the number of components. A metallic baseplate with a low thermal expansion coefficient, such as Invar, is adopted to prevent thermal drift from affecting the measurements. As previously described, the moving mirrors are mounted on the two test masses, while the reference mirror is fixed both to the accelerometer structure and to the spacecraft frame.

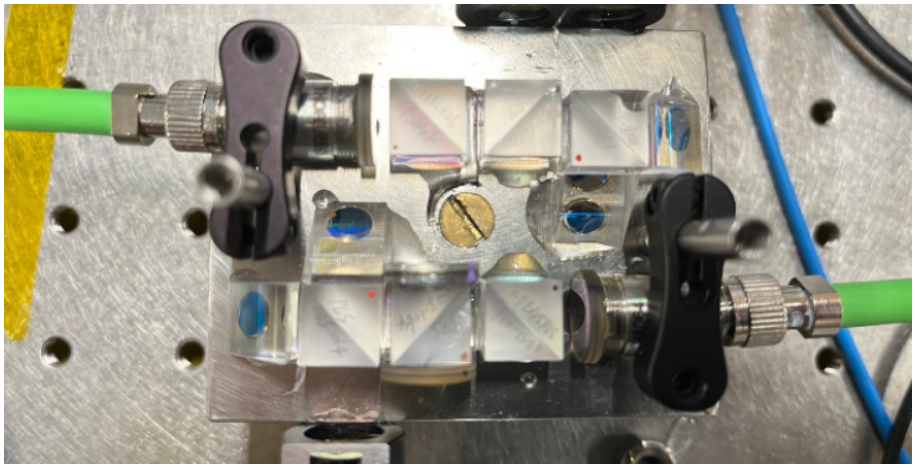

Figure 1.10: Miniaturized evolution of the LIG-A.

Figure 1.11 illustrates the overall layout inside the payload volume $200 \times 200 \times 300$ mm^3 compliant with a M3 platform, which hosts the optical measurement system, optical fibers, and the electronic board. These correspond to the three main LIG-A units described earlier.

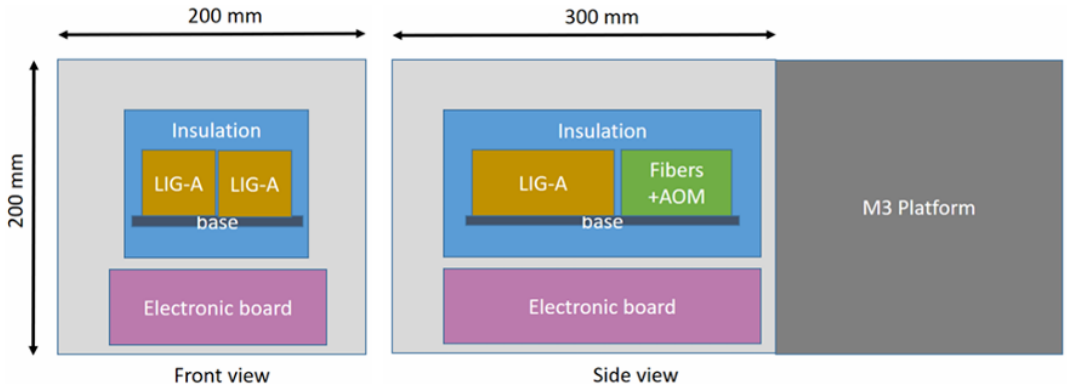

Figure 1.11: Payload layout of the LIG-A CUBE with the M3 platform [10].

Regarding the mass–spring system, ESA required that it be capable of accommodating motion of the test mass in all six degrees of freedom — three translational and three rotational. Although the simultaneous readout of all three axes is not an explicit mission objective, the system has been designed to make this functionality possible. Furthermore, the natural frequency was requested to be as low as possible in order to minimize acceleration noise. An initial target of 0.07 Hz was proposed for the mass–spring system, but this value was later revised to a more realistic upper limit of 1 Hz.

As will be detailed in the following chapter, the design of the elastic suspension system was first developed within the master's thesis project of Ciuffreda [1]. A central objective of the present work is the prototyping of this suspension and the experimental validation of its performance under microgravity conditions, ensuring compliance with the mission requirements.

1.4 Zero Gravity Experiments

The possibility of conducting experiments in microgravity is a crucial aspect in the study of numerous physical, chemical, and biological phenomena. Today, several platforms are available to reproduce weightless conditions, each with specific characteristics in terms of duration, quality of the experimental environment, technical feasibility, and cost.

These platforms can generally be classified into four categories:

- parabolic flights
- drop towers
- suborbital missions
- space stations

Parabolic flights represent one of the most accessible means of achieving short periods of microgravity. In these experiments, an aircraft—such as ESA's A310 ZERO-G or NASA's KC-135—follows a series of parabolic trajectories that generate free-fall conditions inside the cabin. During each parabola, which lasts about 60–65 seconds in total, approximately 20–25 seconds of effective microgravity are achieved. Despite the presence of residual accelerations, this platform allows direct interaction with the experiments and enables multiple runs within a single flight, although each microgravity window remains limited in duration.

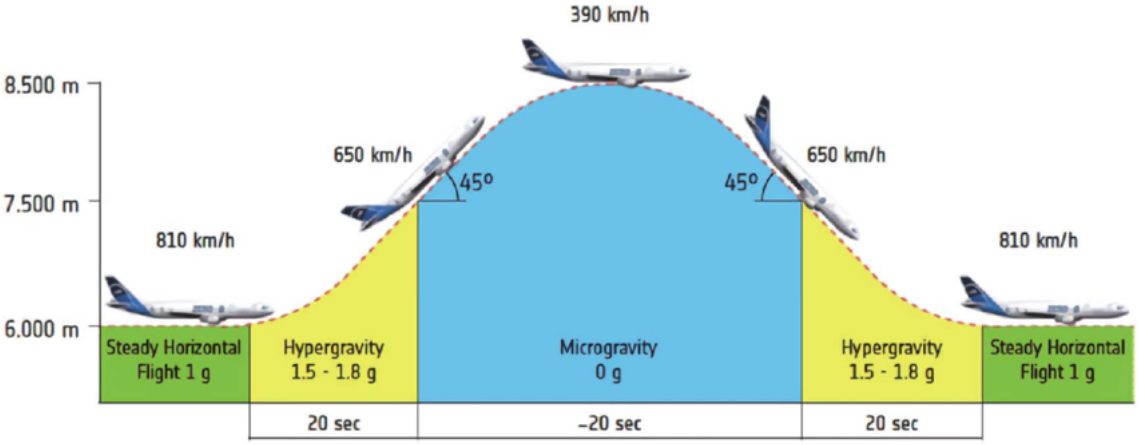

Figure 1.12: Parabolic flight maneuver of the Airbus A310 Zero-G [11].

A ground-based alternative is represented by drop towers, which are vertical structures where experiments are released into free fall inside a vacuum or low-pressure shaft. Some facilities—such as the Einstein Elevator in Hannover—use linear motor systems that launch the experiment upward before it falls, effectively doubling the microgravity path. In this way, test times of up to 4 seconds can be achieved. Drop towers offer a highly controlled environment, with residual accelerations lower than $10^{-6}g$, and are both repeatable and cost-effective. Their main limitations are the short duration of microgravity and the need for full automation of the experimental system.

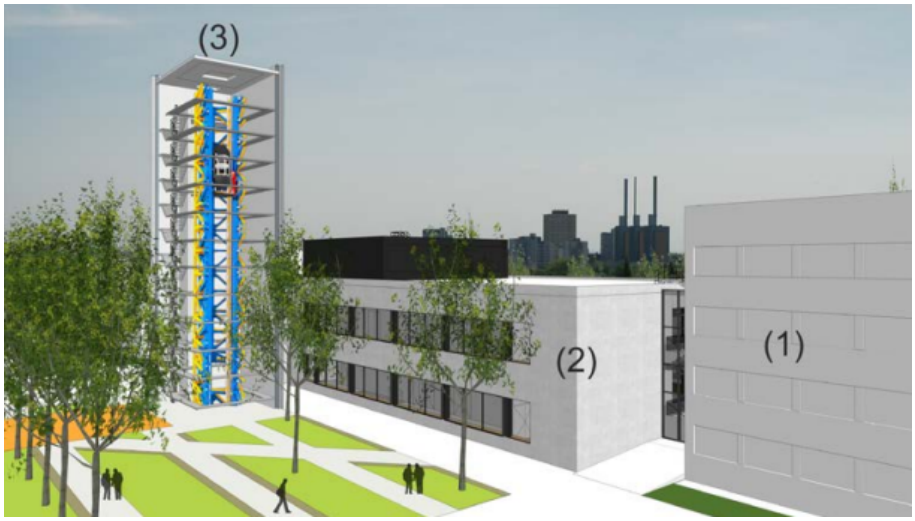

Figure 1.13: Visualization of the Hannover Institute of Technology (HITec) and the Einstein-Elevator within the Hannover skyline. (1) Offices, (2) Laboratory building, (3) Tower building with the Einstein-Elevator [12].

A further advancement is represented by suborbital missions, which involve rocket-launched payloads reaching altitudes above 100 km, thereby crossing the so-called Kármán line. During the ballistic phase—once engine thrust ceases and before atmospheric reentry—it is possible to conduct experiments in microgravity for durations typically ranging from 3 to 5 minutes. Unlike parabolic flights or drop towers, this mode provides access to a near-space environment, including exposure to partial vacuum and space radiation. However, high operational costs, complex logistics, and the inability to interact with the payload during flight are notable drawbacks.

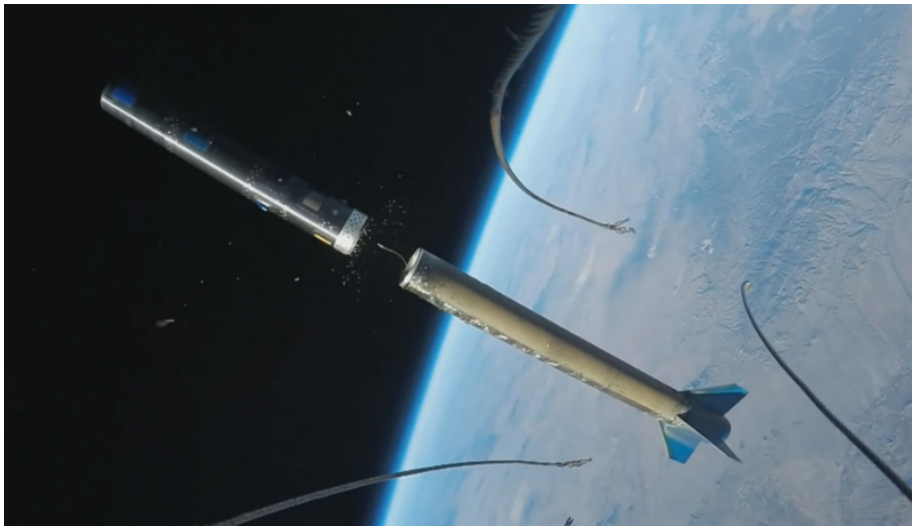

Figure 1.14: Spaceloft XL suborbital vehicle [13].

Finally, long-term microgravity conditions can be achieved aboard space stations in low Earth orbit, such as the International Space Station (ISS). In this context, microgravity is sustained continuously over extended periods—ranging from weeks to months—allowing the investigation of long-duration effects, particularly in the fields of medicine, cellular biology, and materials science. Furthermore, the presence of astronauts on board enables real-time monitoring and manual interaction with experimental setups. Despite these advantages, the extremely high cost, extended planning timelines, and limited access—typically reserved for large-scale international research initiatives—pose significant constraints.

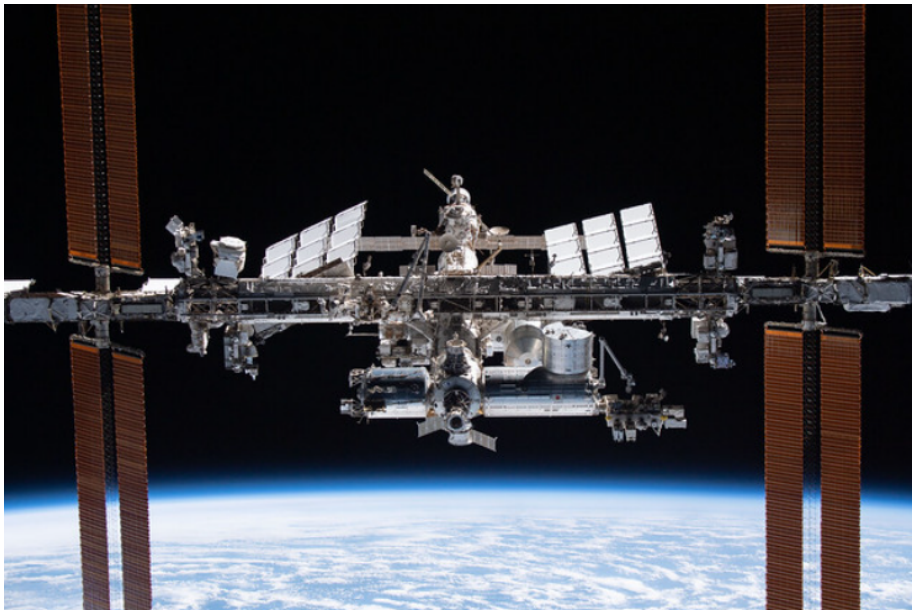

Figure 1.15: International Space Station [14].

In the case of the LIG-A experiment, the drop tower was selected as the preferred microgravity platform. This choice was primarily motivated by the high level of experimental repeatability and the relatively low cost compared to other available options, which made the testing campaign more accessible. Although each individual drop offers a shorter microgravity window than other platforms, the possibility of performing a large number of consecutive launches compensates for this limitation and enables robust statistical validation of the results.

Following a recommendation by ESA, the specific facility used in this project is the *Einstein Elevator*, located at the Hannover Institute of Technology (HITec) of the Leibniz University Hannover. It is an active drop tower that employs a linear-motor-based drive system to enable both upward and downward catapulted motion within a 36-meter vertical shaft. The elevator is capable of achieving microgravity levels below $10^{-6}g$ for up to 4 seconds, while maintaining full environmental control (e.g., pressure, temperature, humidity). Moreover, it can also simulate reduced-gravity conditions such as lunar gravity ($0.165\,g$) and Martian gravity ($0.376\,g$).

A more detailed description of the Einstein Elevator and the experimental setup adopted in this project is provided in the Appendix.

Summary of the Results from the Previous Project

According to the mission requirements, specifically the need to reduce the first natural frequency to below 1 Hz, two alternative design solutions were analyzed and evaluated in the previous thesis project [1].

The first proposed solution is based on the HELI-CAL® Type technology, an elastic element commonly used in flexible couplings to compensate for misalignments between rotating shafts. This type of coupling is made from a single cylindrical metal block, typically stainless steel or high-performance alloys, which is machined using CNC(Computer Numerical Control) helical cutting. The cutting process creates a continuous helical pattern that allows the component to elastically deform across multiple degrees of freedom, while maintaining high structural integrity and fatigue resistance.

HELI-CAL technology is widely used in high-precision applications, including scientific instruments and devices for space environments, due to its ability to ensure repeatable mechanical performance and stable dynamic behavior even under extreme conditions.

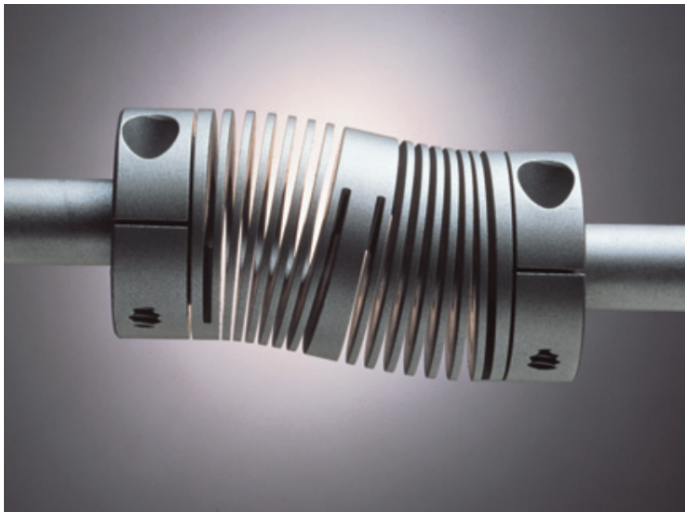

Figure 2.1: Mondial HELI-CAL® [15] beam coupling for parallel misalignments.

The second proposed solution consists of a multiple sheets elastic suspension. The working principle of this configuration relies on a set of thin metal sheets arranged to support the mass through a crossed connection. The sheets are riveted together at alternating corners to ensure significant bending stiffness in both principal directions of the plane. This configuration enables precise control of the relative motion between the mass and the frame, limiting undesired degrees of freedom and improving overall system stability. A schematic example of the concept is shown in the Figure 2.2 and the prototype in Figure 2.3.

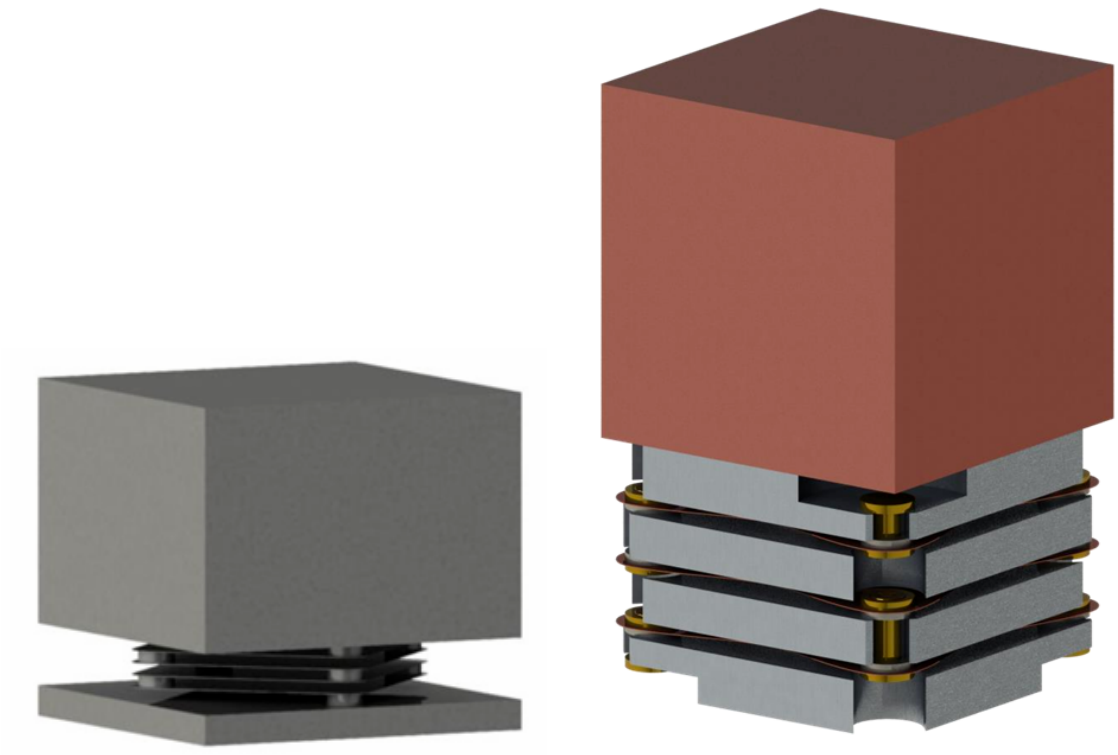

a) b)

Figure 2.2: a) Rendering of the multi-sheet elastic suspension; b) Rendering of the prototype structure.

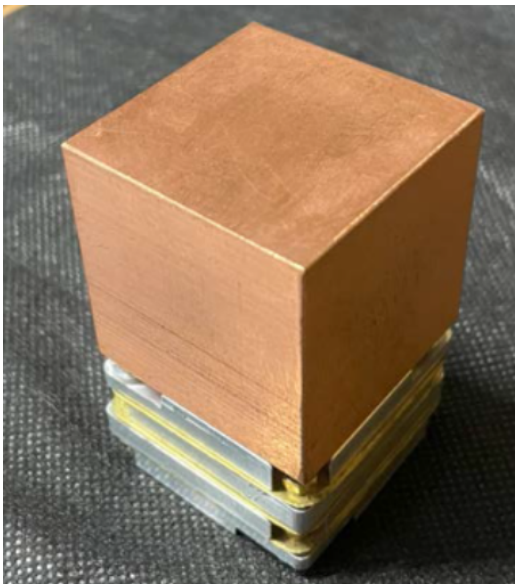

Figure 2.3: Multiple sheets prototype.

Although a detailed study was carried out on the second architecture, the present thesis focuses on the development of the HELI-CAL-based prototype produced using additive manufacturing (AM) techniques. This choice is motivated by the superior mechanical performance of the latter. The main advantages of this solution include:

- absence of mechanical joints or welds, reducing assembly tolerances and increasing reliability;
- linear and tunable mechanical response depending on the geometry of the helical cut (pitch, depth, number of coils);
- compactness and ease of integration into complex mechatronic systems.

2.1 HELI-CAL Model

Figure 2.4 shows the final geometry of the proposed prototype [1], determined through finite element simulation of its dynamic and static behavior. The configuration consists of a cubic mass with 40 mm sides, made of beryllium copper alloy C17200, and a spring made of titanium alloy R58153. The spring is composed of two identical, counter-wound helices in order to decouple the torsional and the longitudinal degrees of freedom, each with 10.5 turns of 0.5 mm wire and a pitch of 1 mm.

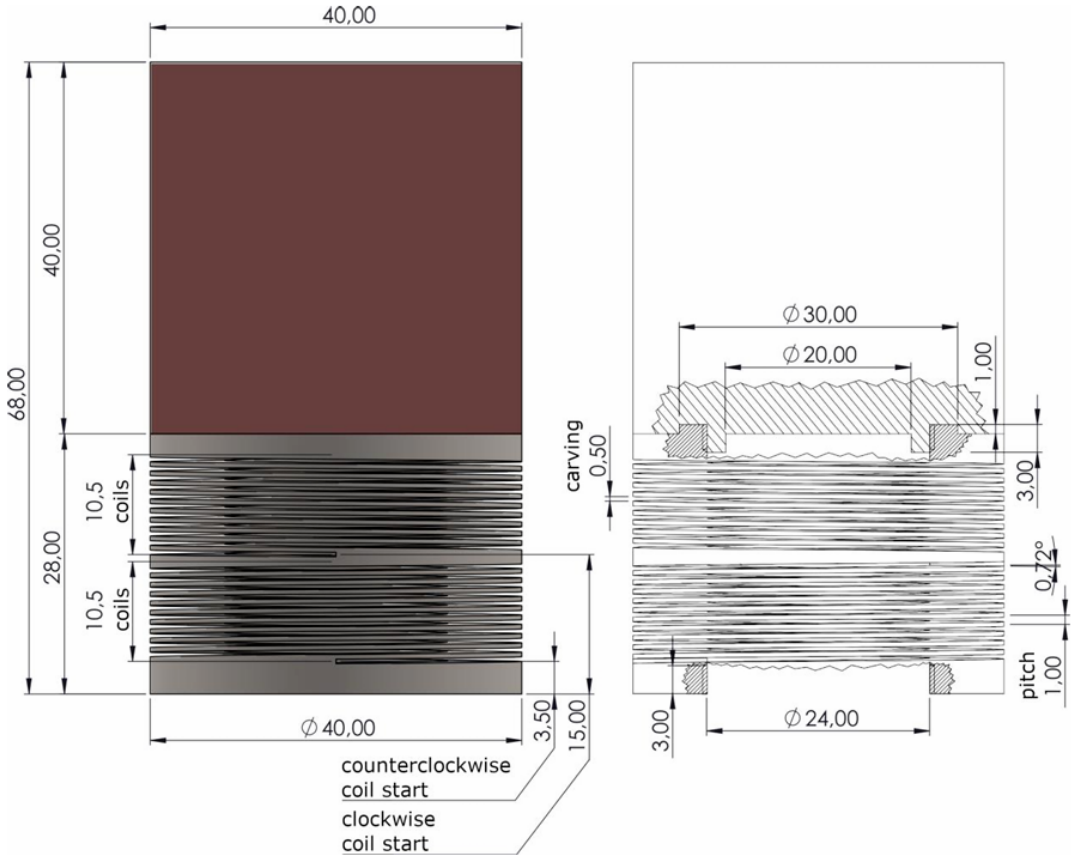

Figure 2.4: Dimensioned CAD of proposed suspension system [1].

Design and Prototyping of the Elastic Suspension

As previously mentioned, the HELI-CAL type elastic suspension was manufactured using AM in collaboration with IAM@Polito. This advanced fabrication method was chosen because of its ability to produce geometrically complex components with high precision and design flexibility—advantages particularly relevant for aerospace applications.

The specific AM process adopted was Powder Bed Fusion with Laser Beam (PBF-LB). The prototype was produced using a Trumpf TruPrint 1000 G06 machine (Figure 3.1), a medium-sized system with a build volume of 98 × 100 mm, diameter × height. The system is equipped with a high-performance fiber laser with a power of up to 200 W and a beam spot size of 80 µm, which enables the fabrication of extremely small and detailed features.

Figure 3.1: Trumpf TruPrint 1000.

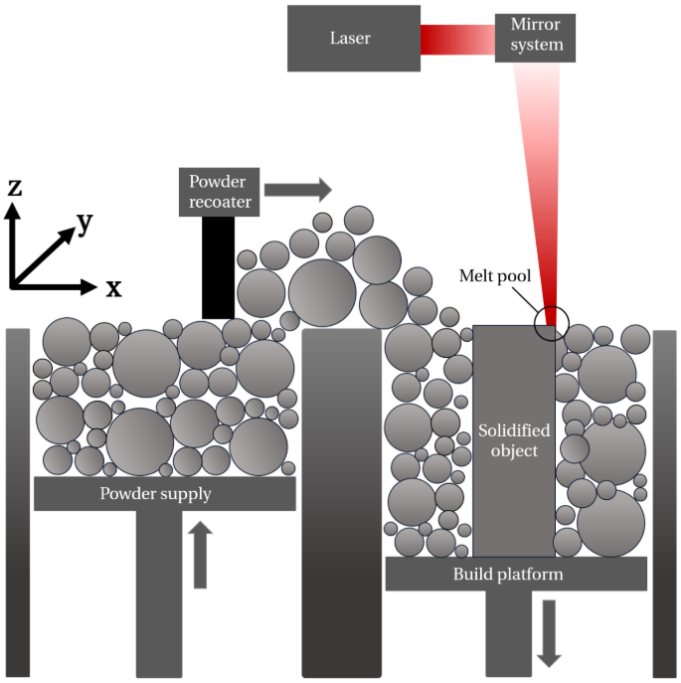

Figure 3.2: Schematic representation of the PBF-LB process [16].

The PBF-LB process, schematized in Figure 3.2, is a layer-by-layer additive manufacturing technique in which a recoater spreads a thin layer of powder uniformly across a build platform. A high-power laser then selectively melts the powder based on the part geometry for that layer, as defined in the CAD model. After each layer is processed, the build platform lowers by a fixed layer height, while the platform inside the powder reservoir rises to supply new material. This synchronized movement allows the recoater to distribute a fresh layer of powder and repeat the cycle, progressively building the component upward. The entire process is carried out in an inert gas atmosphere to protect the material from oxidation and thermal degradation during laser exposure. The TruPrint 1000 system supports both argon and nitrogen environments; in this particular case, argon was used during the printing of the prototype.

The main process parameters influencing the PBF-LB are the laser power (P), the scan speed (v), and the hatch spacing (h), which refers to the distance between adjacent lines of fused.

The approach used for the prototyping of the elastic suspension is as follows: Job 1, in which a feasibility study is conducted using a non-final material, along with a preliminary characterization to assess the feasibility of the required geometry. Next, the material to be used for the prototype is selected. This is followed by Job 2, in which two main objectives are pursued: the definition of the process parameters on coupons that are thin metal sheets, aimed at minimizing defects by selecting appropriate process parameters, and the design of the support structures on half coils of the spring.

Then, in Job 3, samples representing springs with a reduced number of coils are produced to evaluate the characteristics of the suspension. Afterward, the samples are characterized, and the final geometry is selected. The process ends with Job 4, namely the production of the final prototype.

3.1 Modifications from the Original Model

Based on the proposed geometry, several modifications were introduced both in the test mass and in the spring to enable proper assembly onto the test bench. Specifically, a 6 mm diameter hole was added to the mass, while the spring was modified on one end with M4 holes to be tapped to mount it to the test bench, and on the opposite end with a central through-hole of 6 mm diameter—identical to that in the mass—to allow the two components to be joined together. Around this central hole, additional smaller through-holes were introduced to provide, if necessary, a more rigid constraint between the two components, as shown in Figures 3.3.

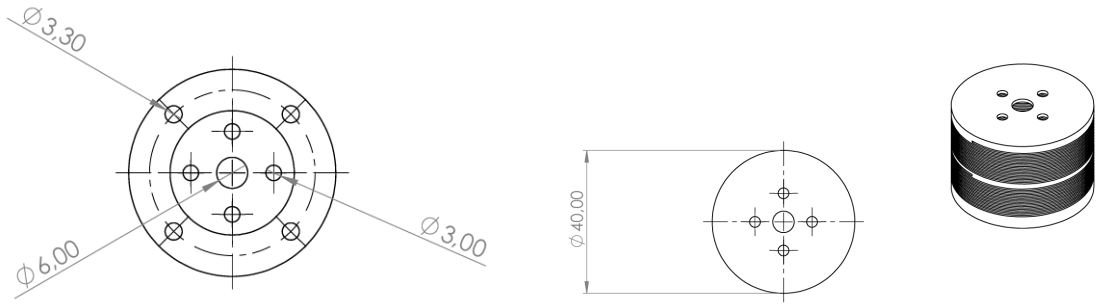

a) b)

Figure 3.3: a) Technical Drawing: Lower View of the Spring; b) Technical Drawing: Upper View of the Spring.

Following these modifications, a modal finite element analysis was carried out using ANSYS software in order to validate the results obtained in the previous project, namely the achievement of bending natural frequencies below 1Hz.
In the simulation, the mass was modeled using beryllium copper alloy C17200 and discretized with an automatic mesh, where an Element Size (E-Size) of 4 mm was specified. The E-Size defines the target length of the edges of the finite elements in the mesh and directly affects both the accuracy and computational cost of the analysis.

For the spring component, a titanium alloy (Ti-6Al-4V) was used, which is also the final material selected for the prototype, as will be discussed in the next chapter. The geometry was discretized with an E-Size of 2.4 mm to accurately capture the fine structural features of the helical design. Furthermore, to prevent the occurrence of rigid body modes, a fixed support was applied to the lower face of the spring, corresponding to its actual physical constraint.

Table 3.1 summarizes the material properties used for the simulation.

Table 3.1: Material properties used in the FEM simulations.

Property	**C17200 (Be-Cu)**	**Ti-6Al-4V**	**Unit**
Density (ρ)	8.25	4.43	g/cm^3
Young's Modulus (E)	130	110	GPa
Poisson's Ratio (ν)	0.30	0.31	–

The simulation returned the expected results, confirming that the first two bending modes occur below 1 Hz, as summarized in Table 3.2.
Figures 3.4a, 3.4b, and 3.5 show, respectively, the first and second bending modes and the first axial mode.

Table 3.2: Modal frequencies obtained from the FEM simulation.

Mode Type	**Frequency [Hz]**
First bending mode	0.46
Second bending mode	0.46
First axial mode	1.25

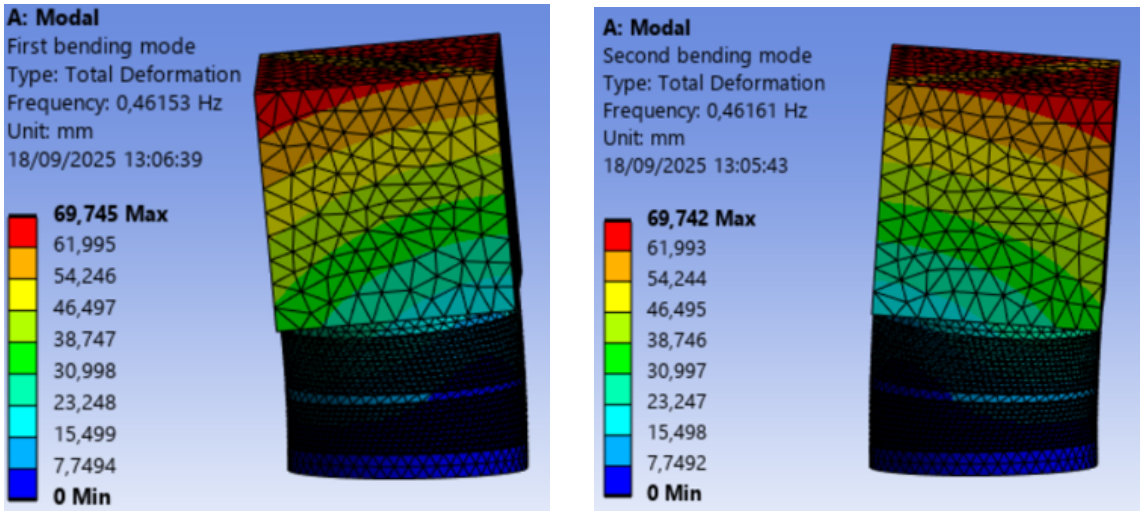

a) b)

Figure 3.4: a) First bending mode; b) Second bending mode.

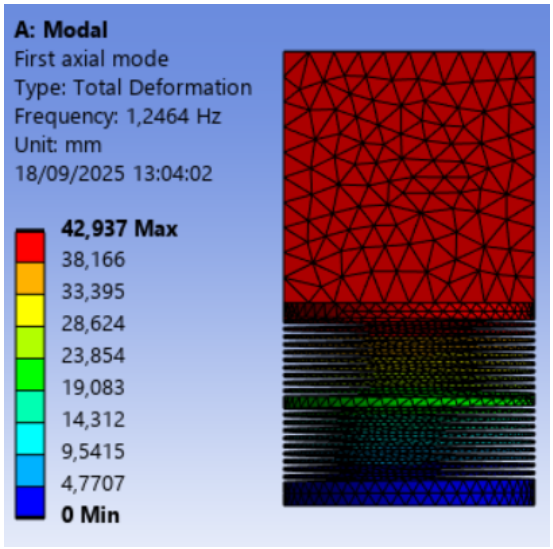

Figure 3.5: First axial mode.

3.2 Job 1:Feasibility Study of the Geometry

The feasibility study was necessary to verify whether the geometry was suitable for this type of AM process. In particular, the aim was to assess whether the small coil thickness of 0.5 mm—which is one of the distinctive features of this geometry—could be adequately produced. As previously mentioned, the material used for Job 1 was not the final one. Instead, an aluminium alloy was selected, specifically AlSi10Mg, which is also suitable for space applications.

The first test print for the Job 1 was then performed, using the standard process parameters for this material. These parameters are reported in Table 3.3.

Table 3.3: Process parameters used for Job 1 with AlSi10Mg.

Parameter	**Value**
P	200 W
v	80 mm/s
h	130 μm

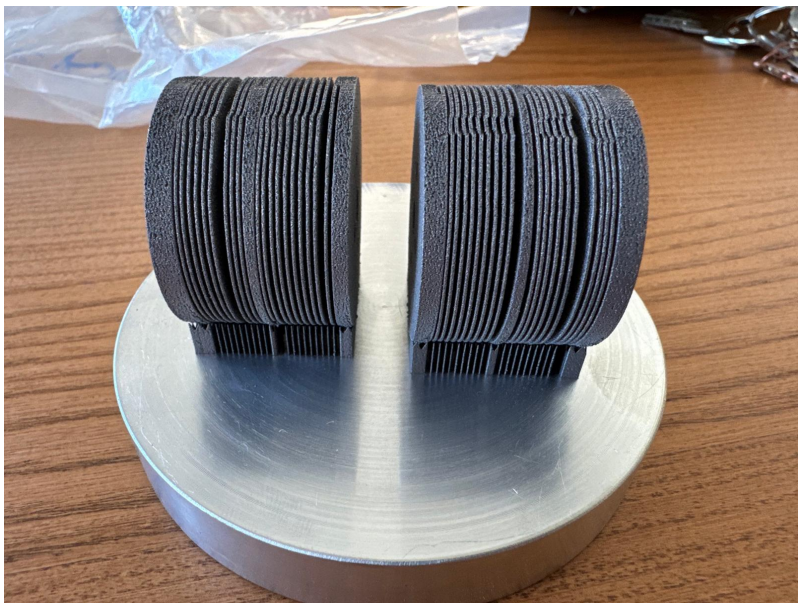

Figure 3.6: Job 1.

As shown in Figure 3.6, the geometry can be successfully reproduced; however, several issues were observed: significant distortions between the coils, a noticeable misalignment in the upper part of the coil—an issue that was also encountered in Job 1 and whose resolution will be discussed later—and high porosity.

3.2.1 Dynamic Analysis

After printing the aluminium alloy spring to verify the feasibility of the geometry, a dynamic analysis was carried out on the prototype to experimentally determine its flexural and axial natural frequencies. The results were then compared with a finite element analysis.

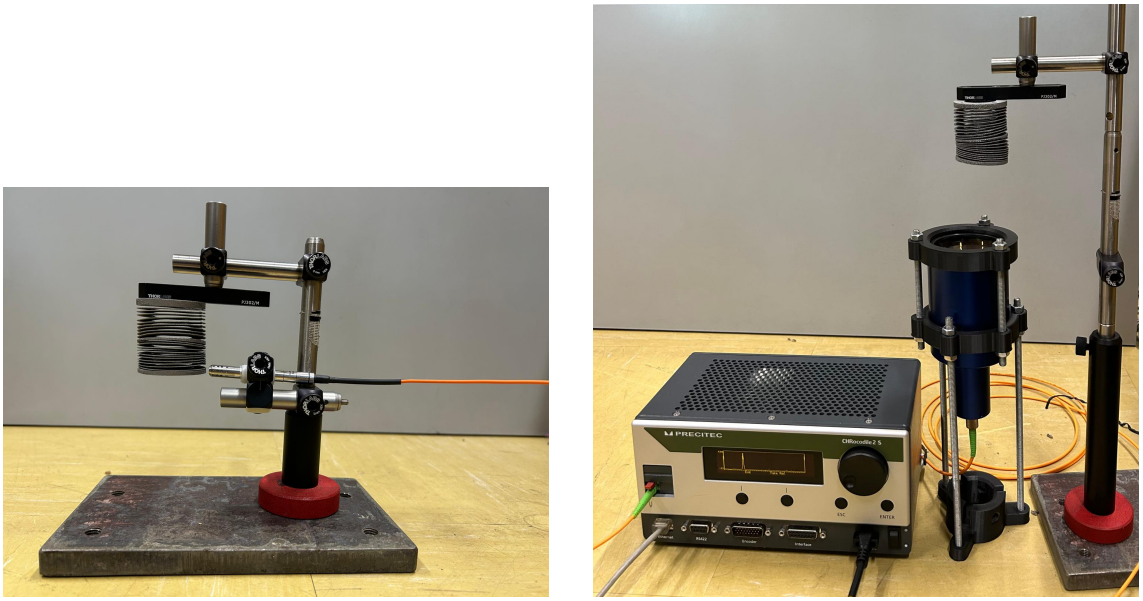

a) b)

Figure 3.7: a) Transverse displacement measurement; b) Axial displacement measurement.

From an experimental standpoint, the oscillations of the spring — mounted at one end and free at the other — were monitored, as shown in Figures 3.7a and 3.7b. Both transverse and axial oscillations were measured.

The measurement was performed using a Precitec CHRocodile 2S device, which

operates on the principle of chromatic confocal sensing. This technique combines two physical phenomena:

- Chromatic dispersion, in which a white light beam is dispersed by a chromatic lens so that each wavelength, corresponding to a specific colour, is focused at a different position along the optical axis.
- Confocal detection, in which only the light perfectly focused on the surface is reflected back with sufficient intensity to be detected by the sensor.

This measurement approach offers several advantages: high precision, applicability to rough or inclined surfaces, the ability to measure transparent materials such as glass, contactless operation eliminating the risk of damaging the part, independence from the material type, and very high resolution down to nanometres depending on the probe used.

Two different probes were employed in the measurements:

- For the transverse displacement measurements, a probe with a measurement range of ± 100 μm and focal depth of 1.4 mm was used.
- For the axial displacement measurements, a second probe was employed, featuring a larger range and a greater focal depth approximately 15 mm and 65 mm respectively, required due to the higher amplitude of axial oscillations.

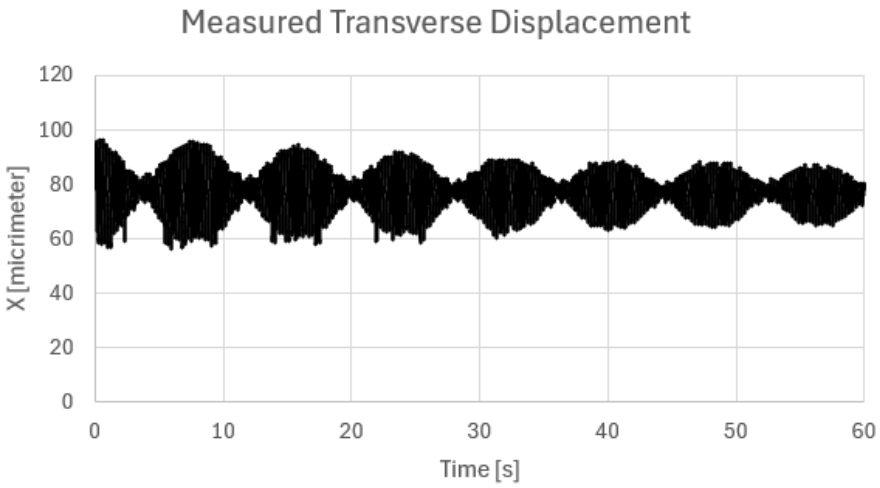

Figure 3.8: Measured transverse displacement.

Figure 3.8 shows the measured transverse displacement. A beating effect is clearly visible, caused by the coupling of flexural modes at close frequencies. To analyse this behaviour, the Power Spectrum of the displacement signal was computed using a Fast Fourier Transform based algorithm developed in Labview environment,

The double-logarithmic power spectrum of the transverse displacement, Figure 3.9a, shows three main peaks: two close peaks at 3.83 Hz and 3.95 Hz representing the first and second flexural modes, responsible for the beating, and a smaller peak at 4.68 Hz corresponding to the first axial mode. This axial mode appears in the transverse measurement due to the coupling between modes.

Subsequently, the axial displacement measurement was carried out with the second probe. The resulting double-logarithmic power spectrum (Figure 3.9b) confirmed the presence of a small peak at approximately 3.80 Hz and a dominant peak at 4.68 Hz, consistent with the first axial mode.

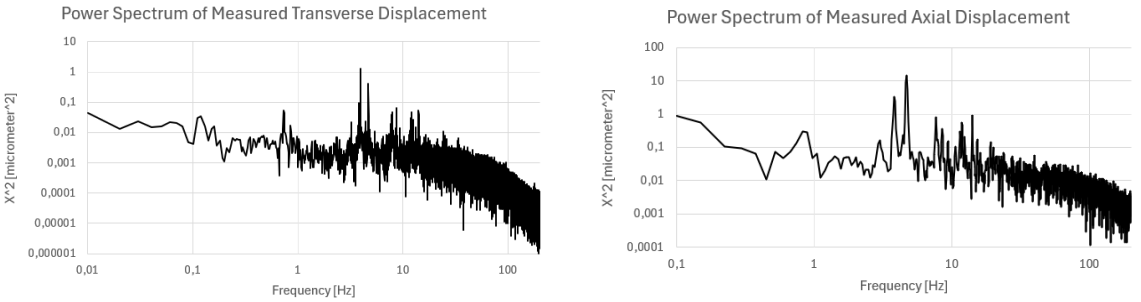

a) b)

Figure 3.9: a) Power spectrum of measured transverse displacement; b) Power spectrum of measured axial displacement.

In addition to the frequency response analysis of the spring, a qualitative estimation of the time constant τ and the damping ratio ζ was carried out for both flexural and axial oscillations. This estimation was performed by considering three pairs of peaks, as shown in Figure 3.10a and 3.10b, using the logarithmic decrement method and then averaging the values obtained for these three pairs. Because the presence of beating invalidates the method, the system was idealized by assuming the two bending frequencies to be coincident, in order to obtain an order-of-magnitude estimate of τ and ζ.

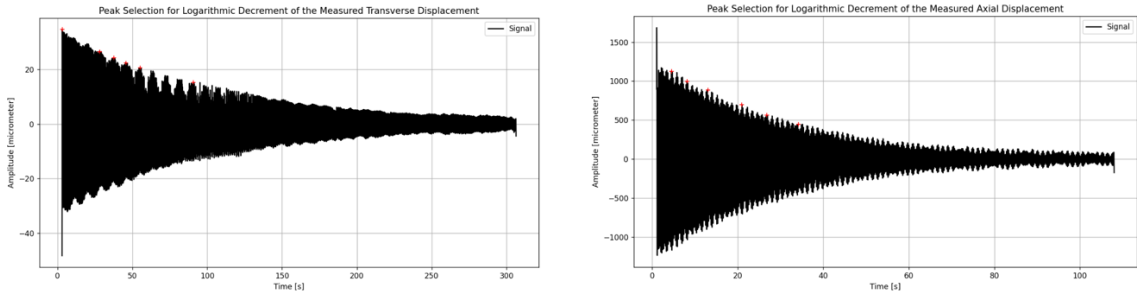

a) b)

Figure 3.10: Peaks used to estimate the transverse (a) and the axial (b) damping ratio and time constant;

The formulas used are:

$$\delta = \frac{1}{n} \ln\left(\frac{x_1}{x_2}\right) \tag{3.1}$$

$$\zeta = \frac{\delta}{\sqrt{(2\pi)^2 + \delta^2}} \tag{3.2}$$

$$\omega_n = \frac{\omega_d}{\sqrt{1 - \zeta^2}} \tag{3.3}$$

$$\tau = \frac{1}{\zeta\, \omega_n} \tag{3.4}$$

where:

- x_1 and x_2 are the amplitudes of two consecutive peaks,
- n is the number of cycles between the two peaks,
- δ is the logarithmic decrement,
- ω_d is the damped angular frequency, obtained from the spectral analysis,
- ω_n is the undamped natural angular frequency,
- τ is the time constant.

The results of this estimation are reported in Table 3.4.

Table 3.4: Average results of the damping ratio ζ and the time constant τ.

Parameter	**Transverse oscillations**	**Axial oscillations**	**Unit**
Time constant (τ_{avg})	$\sim 10^3$	$\sim 10^2$	s
Damping ratio (ζ_{avg})	$\sim 10^{-4}$	$\sim 10^{-3}$	–

3.2.2 Modal Analysis with Finite Elements

An FEM analysis of the spring was also performed to compare the results with the experimental measurements. The material properties used in the FEM simulations are reported in Table 3.5, where the density corresponds to the measured value, while

Young's modulus and Poisson's ratio are the standard values for the aluminium alloy AlSi10Mg.

Figure 3.11a shows the mesh used for the simulations, while Figures 3.11b, 3.11c and 3.11d show the first and second bending modes and the axial mode respectively.

Table 3.5: Material properties used in the FEM simulations of the spring.

Property	**Value**	**Unit**
Density (ρ)	2.36	g/cm^3
Young's Modulus (E)	70	GPa
Poisson's Ratio (ν)	0.30	–

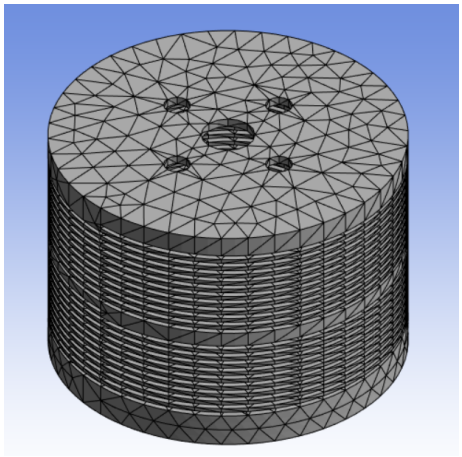

a)

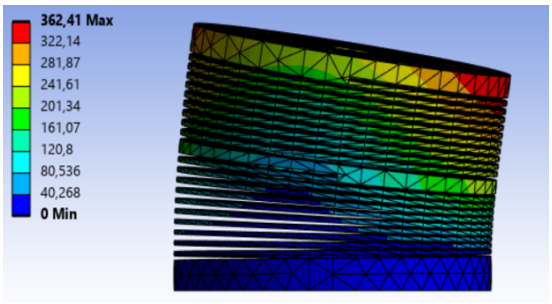

b)

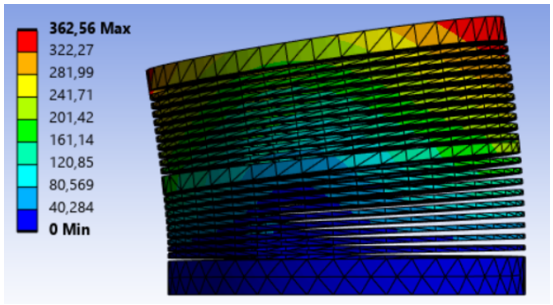

c)

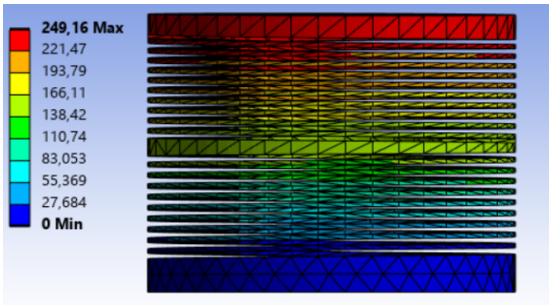

d)

Figure 3.11: a) Mesh of the spring; b) First bending mode; c) Second bending mode; d) First axial mode.

In particular, a convergence analysis was carried out. As shown in the Figures below, the first flexural mode converges to approximately 5.18 Hz, the second flexural mode to 5.19 Hz, and the first axial mode to 6.21 Hz.

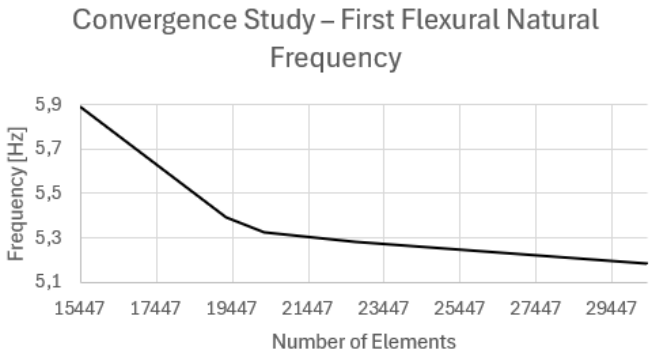

Figure 3.12: Convergence of the first bending mode of AlSi10Mg spring.

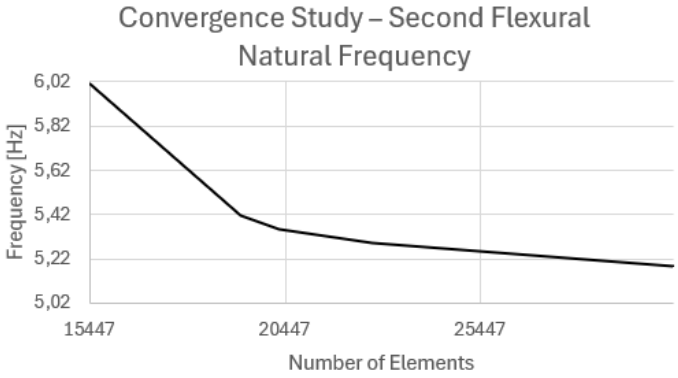

Figure 3.13: Convergence of the second bending mode AlSi10Mg spring.

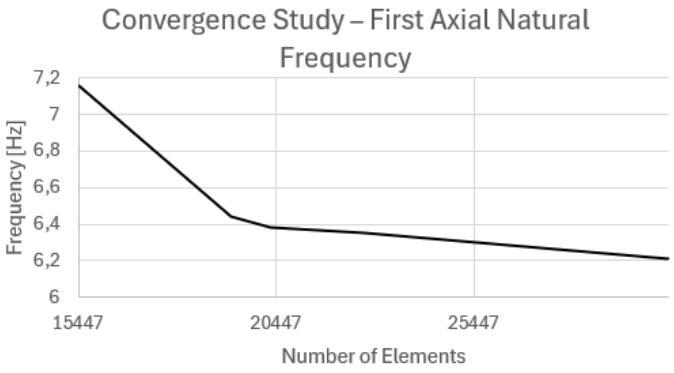

Figure 3.14: Convergence of the first axial mode AlSi10Mg spring.

Table 3.6 summarizes the results obtained from both the experimental tests and the FEM simulations. By analyzing the first three natural frequencies, it can be observed that the measured values are consistently lower than the simulated ones by approximately 1.25–1.53 Hz. This uniform discrepancy suggests the presence of a systematic error in the numerical model, likely related to an overestimation of the structural stiffness and the actual Young's modulus. Such overestimation may be attributed to factors including diffuse porosity, residual stresses not accounted for in the FEM model, local plastic deformations, and non-ideal boundary conditions compared to the idealized constraints used in the simulations.

Table 3.6: Comparison between measured and FEM natural frequencies of the spring.

Mode	**Measured frequencies[Hz]**	**FEM frequencies[Hz]**
First flexural mode	3.93	5.18
Second flexural mode	3.95	5.19
First axial mode	4.68	6.21

3.3 Material Selection

The choice of material plays a crucial role in space applications. For the selected additive manufacturing technique, PBF-LB, the most commonly used materials are the titanium alloy Ti-6Al-4V, the aluminum alloy AlSi10Mg, adopted in the Job 1, nickel-based superalloys, and stainless steels such as 316L. The main properties of these materials are summarized in Table 3.7.

In particular, aluminum alloys are widely used because of their low density and good thermal properties, although they lack high ductility. Nickel-based superalloys are characterized by excellent strength at elevated temperatures, up to 1000°C, making them suitable for engines and nozzles. Stainless steels, on the other hand, are easy to process by additive manufacturing and offer good ductility, but they are generally employed for secondary components. Finally, the titanium alloy Ti-6Al-4V is extensively used by NASA and ESA due to its excellent strength-to-weight ratio. This alloy combines high mechanical strength with good ductility, which is particularly advantageous for the main objective of this thesis that is lowering the natural frequencies of the system. For this reason, titanium was selected as the reference material for the continuation of the study on the elastic suspension.

Table 3.7: Main properties of alloys commonly used in PBF-LB for space applications.

Material	ρ	**E**	**UTS**	**k**	$\mathbf{T_{max}}$	**Reference**
	[g/cm^3]	[GPa]	[MPa]	[W/mK]	[°C]	
Ti-6Al-4V	4.43	110	900–1100	6.7	400–500	[17]
AlSi10Mg	2.68	70	400–500	120–150	200–250	[18]
Ni-based superalloy (IN718)	8.19	200	1200–1400	11–15	800–1000	[19]
Stainless steel 316L	8.00	190	500–700	15–20	600–700	[20]

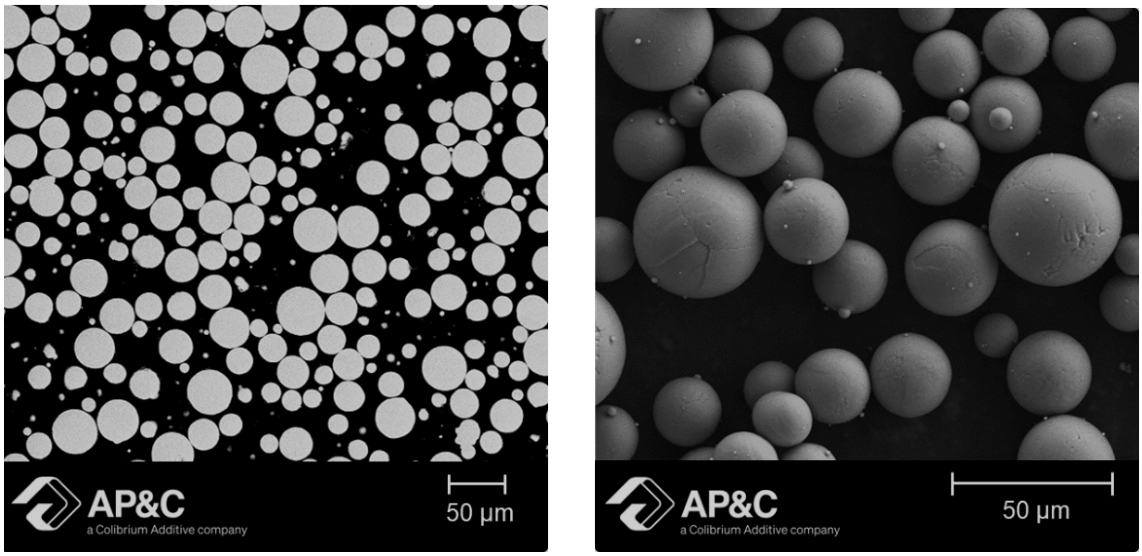

a) b)

Figure 3.15: a) Metallographic images [21]; b) Particle size distribution[21].

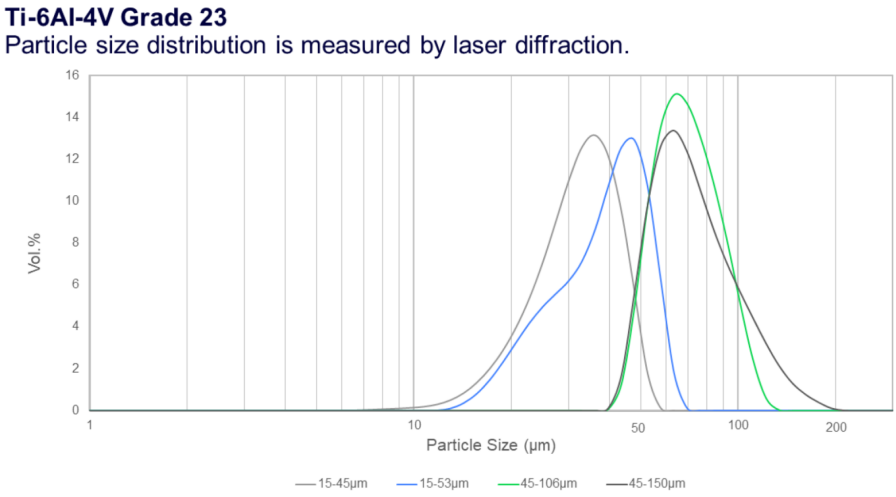

Figure 3.16: Ti-6Al-4V grade 23 particle size distribution [21].

In particular, a Ti-6Al-4V grade 23 powder with a particle size distribution of 15–45 μm, supplied by Advanced Powder and Coatings (AP&C), was adopted. Figure 3.15a shows the metallographic distribution, while Figure 3.15b and the grey line in Figure 3.16 illustrate the particle size distribution. The main mechanical properties of the alloy, as reported by the manufacturer, are summarised in Table 3.8.

Table 3.8: Mechanical properties of Ti-6Al-4V grade 23 powder (15–45 μm) provided by AP&C.

Property	**Value**	**Unit**
Apparent density	2.49	g/cm^3
Theoretical density	4.43	g/cm^3
Young's modulus (E)	110	GPa
Poisson's ratio (ν)	0.31	–
Yield strength (YS)	795–860	MPa
Ultimate tensile strength (UTS)	860–950	MPa

3.4 Job 2: Process Parameter Optimization and Support Design

The main objectives of Job 1 were: the optimisation of the PBF-LB process parameters through a Design of Experiments (DoE) study and the selection of the best settings, and the optimisation of the support geometry, which is a critical aspect for a successful build.

A two-level, three-factor DoE was initially adopted, leading to 2^3 experimental combinations around the standard parameter set for Ti-6Al-4V. Two relative variations were explored with respect to the baseline: $\pm 10\%$ and $\pm 20\%$ (Table 3.9). The factors investigated, as previously mentioned, were:

- laser power P [W],
- scan speed v [mm/s],
- hatch spacing h [mm].

To interpret the results, the following energy-based metrics were monitored:

$$E_\ell = \frac{P}{v} \quad \text{(linear energy density, J/mm)}, \qquad E_v = \frac{P}{v\,h\,t} \quad \text{(volumetric energy density, J/mm}^3\text{)},$$

where t is the layer thickness which was set to 30 μm. Combinations exceeding the maximum laser power of the machine were excluded from the test matrix (from experiment 6 to 9).

Table 3.9: Design of Experiments with ±10% and ±20% variation around baseline parameters.

	±10%					±20%				
Exp.	**P [W]**	**v [mm/s]**	**h [μm]**	**P/v**	**P/(v*h*t)**	**P [W]**	**v [mm/s]**	**h [μm]**	**P/v**	**P/(v*h*t)**
1	200	1500	100	0.13	44.4	200	1500	100	0.13	44.4
2	180	1350	90	0.13	49.4	160	1200	80	0.13	37.0
3	180	1350	110	0.13	40.4	160	1800	90	0.09	37.0
4	180	1650	90	0.11	40.4	160	1800	120	0.09	27.7
5	200	1050	110	0.19	33.1	200	900	120	0.22	46.3
6	220	1350	90	0.16	60.4	240	1200	80	0.20	83.3
7	220	1050	100	0.21	49.6	240	1200	100	0.20	66.7
8	220	1200	90	0.18	49.4	240	1800	90	0.13	55.6
9	220	1650	110	0.13	40.4	240	1500	110	0.13	37.0

Finally, after a review of the literature, the investigation focused on parameters with progressively increasing volumetric energy density 3.17, while maintaining the maximum machine power of 200 W and varying only the hatch distance and the scanning velocity, as illustrated in table 3.10. For experiment 9, the same parameters as in experiment 1 were adopted, with the addition of an upskin setting. This implies that the last layer was processed with different parameters, reported in Table 3.11, which correspond to the standard configuration.

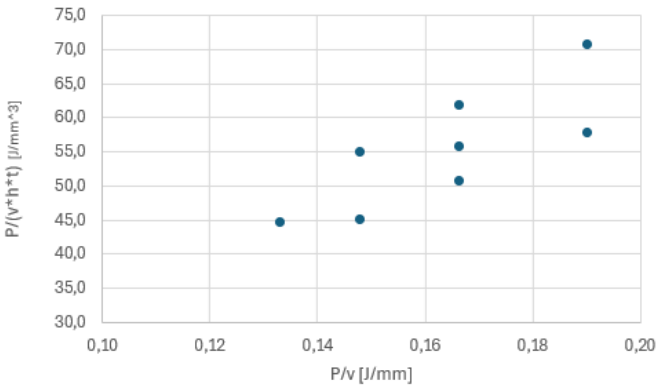

Figure 3.17: Parameters explored with increasing volumetric energy density.

Table 3.10: Process parameters adopted for Job 2.

experiment	**P [W]**	**v [mm/s]**	**h [μm]**	**P/v**	**P/(v*h*t)**
1	200	1500	100	0.13	44.4
2	200	1350	90	0.15	54.9
3	200	1200	90	0.17	61.7
4	200	1350	110	0.15	44.9
5	200	1200	100	0.17	55.6
6	200	1050	90	0.19	70.5
7	200	1050	110	0.19	57.7
8	200	1200	110	0.17	50.5
9 (with upskin)	200	1500	100	0.13	44.4

Table 3.11: Upskin parameters applied in Experiment 9.

Parameter	**Value**
Laser Power	200 W
Scan Speed	1520 mm/s
Hatch Spacing	88 μm

For process-parameter optimisation, flat coupons of 10×12 mm were printed at different thicknesses representative of the nominal coil sections, which are 0.5 mm, 1.5 mm and 3.5 mm. In total, 27 coupons were produced in Job 1.

Instead for support optimisation, half-coil specimens were analysed using the baseline process parameters (experiment 1) while varying the coil pitch to 1.00 mm, 1.25 mm, and 1.50 mm in order to evaluate detachment, bridging and post-processing behaviour.

Table 3.12: Support parameters used for the half-coil specimens.

Parameter	Value
Surface angle	35°
Tooth height	1.5 mm
Tooth width	1.5 mm
Tooth spacing	0.2 mm
Connection height	0.2 mm
Layer thickness	60 μm

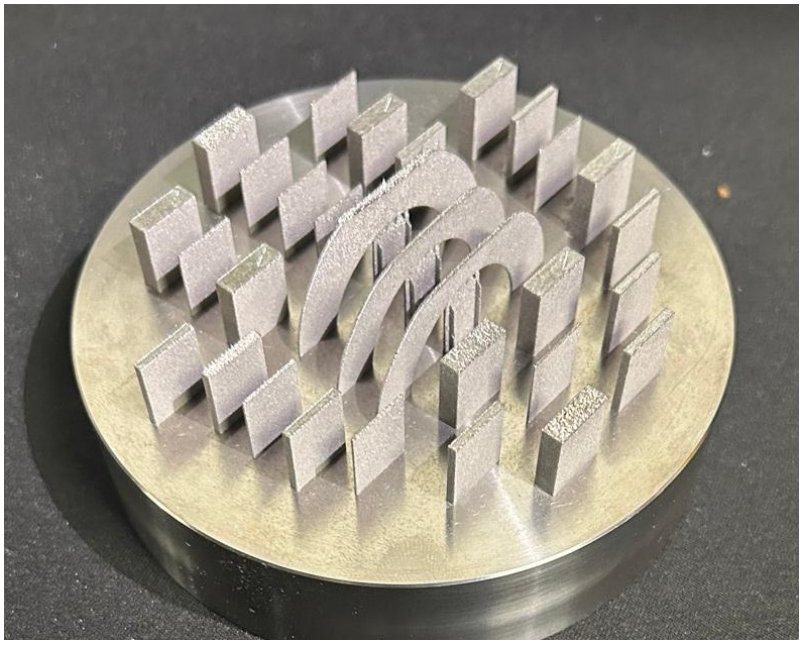

Figure 3.18: Result of the coupon fabrication.

Figure 3.18 shows the result of the coupon fabrication. As can be observed, the build was not successfully completed, particularly with regard to the half-coils. This issue is likely caused by an excessive pressure applied during the spreading of the new powder layer combined with the low stiffness of the part and its supports; in fact, the recoater appeared scratched.

A similar problem had already been encountered in the preliminary study. How-

ever, in that case, since a complete spring was fabricated, the higher stiffness of the structure allowed the build to be completed, though with a misalignment.

This issue could be mitigated by applying a more gradual pressure from the recoater and by properly orienting the spring during the build. In this configuration, the coil axis was arranged perpendicularly to the recoater's movement direction, which may have contributed to the problem.

Another relevant improvement concerns the surface quality; unlike the spring fabricated in aluminum alloy, apparently the process parameters adopted here did not result in high surface roughness or porosity, this issue was confirmed with further analisys .

Finally, the coupons were separated using Wired Electrical Discharge Machining (W-EDM), as shown in Figure 3.19. A tungsten wire was employed together with dielectric fluid, which served both to cool the system and to increase electrical conductivity. Moreover, a gap of 0.3 mm from the build plate was set.

Following the process, it was observed that, due to inadequate support design, the supports detached spontaneously during the W-EDM operation. This phenomenon can be attributed to residual stresses in the specimens, since no stress-relief heat treatment had been performed.

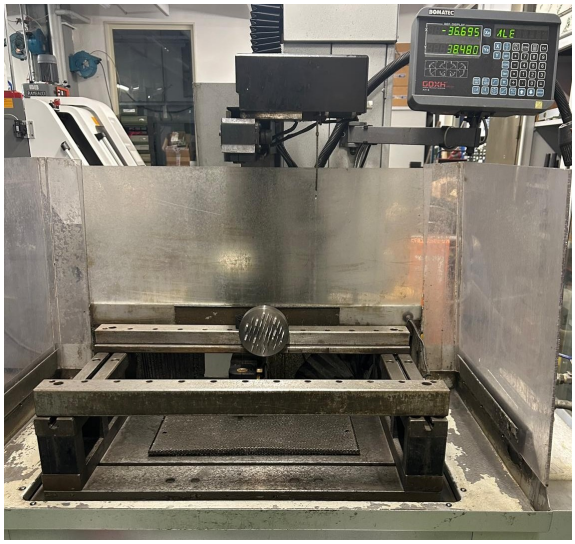

Figure 3.19: Electrical discharge machining process.

3.4.1 Porosity and Roughness Analysis

An important aspect in the selection of the process was the analysis of porosity and surface roughness of the coupons. A non-destructive method was adopted, namely X-ray Computed Tomography (CT), which enables the reconstruction of the internal structure of a component.

Specifically, three samples were analyzed: the coupons with thicknesses of 0.5 mm and 3.5 mm from Experiment 1, and the coupon with a thickness of 3.5 mm from Experiment 6. These specimens were selected as they correspond to the cases with the lowest and highest volumetric energy density, respectively.

The CT software provides as output both the maximum defect size and the estimated probability that it actually corresponds to an internal cavity, based on X-ray attenuation variations.

The results show no significant internal porosity. Figure 3.20 reports the outcome for the 0.5 mm plate. In particular, the maximum pore diameter detected was 0.11 mm for the 0.5 mm plate and 0.18 mm for the 3.5 mm plate of Experiment 1, while a maximum diameter of 0.21 mm was observed for the 3.5 mm plate of Experiment 6.

In all cases, the probability of defect presence remained very low, below 2.27%, thus confirming that the porosity level is negligible.

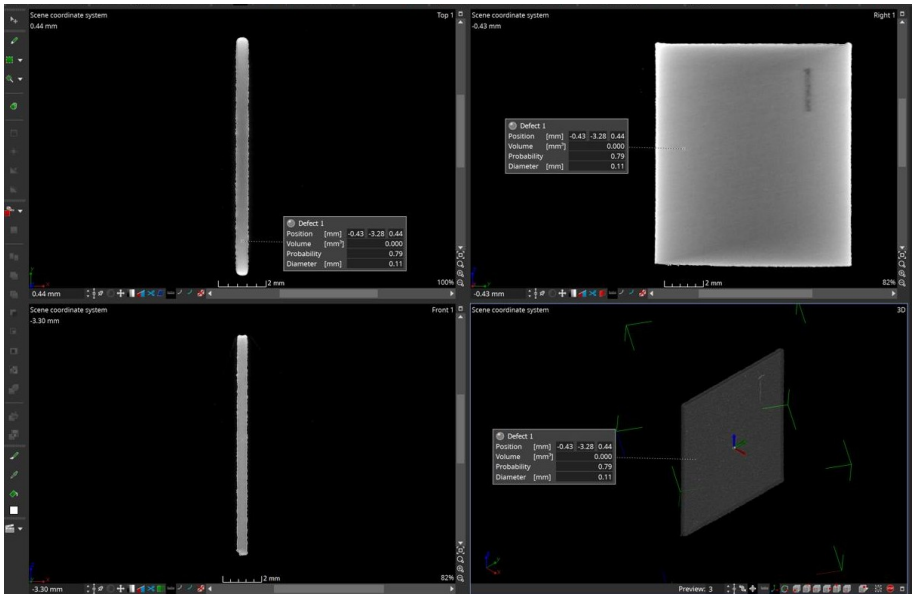

Figure 3.20: CT analysis – Experiment 1, thickness 0.5 mm.

Regarding the roughness analysis, a comparison was carried out between the nominal CAD geometry and the actual geometry obtained from CT scans, using the GOM Inspect software. The results are shown in Figures 3.21a, 3.21b, and 3.21c. In these Figures, the scale on the right represents the geometric deviation in millimeters between the CT-derived surface and the nominal CAD model.

The analysis indicates an overall good quality, with a symmetric distribution of deviations, which makes the result acceptable in all three cases.

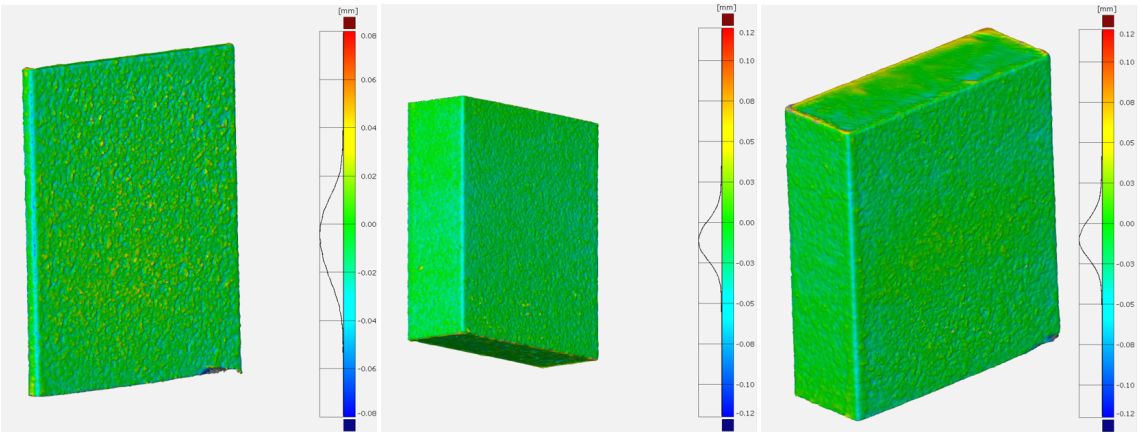

a) b) c)

Figure 3.21: Comparison with nominal geometry – Exp. 1, 0.5 mm (a); - Exp. 1, 3.5 mm (b) ; - Exp. 6, 3.5 mm (c).

3.4.2 Statistical Analysis of Real Dimensions and Parameter Selection

In order to define the final parameters for the production of simplified prototypes, presented in the following section, dimensional measurements were carried out on the coupons. Specifically, three repeated measurements were performed with a caliper on the plates to evaluate thickness and width, while for the half coils three measurements were taken of the coil width, defined as the difference between the external and internal radius. The data were then processed through a statistical analysis.

Figures 3.22 and 3.23 illustrate the main effects on the deviations of thickness (t) and width (w), where Δ indicates the difference between the measured and the nominal value. The results highlight that the plate thickness is, on average, slightly higher than the nominal value, with a mean deviation of approximately $+0.03\,\text{mm}$, whereas the plate width is generally lower, with a mean deviation of about $-0.05\,\text{mm}$. No significant influence of the process parameters was observed. Only in the case of coil width a marginal effect of the scan speed was detected, as the deviation tends to increase slightly at higher scanning velocities, possibly due to the reduced linear energy input. For plate thickness, deviations appeared to be

more pronounced in the 0.5 mm samples.

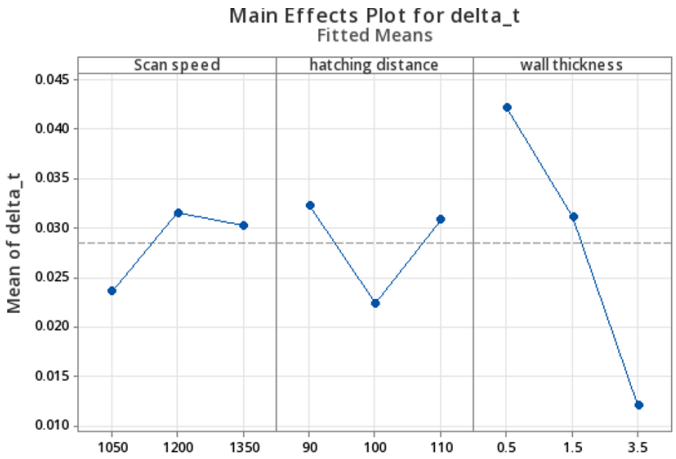

Figure 3.22: Main effects on thickness (t).

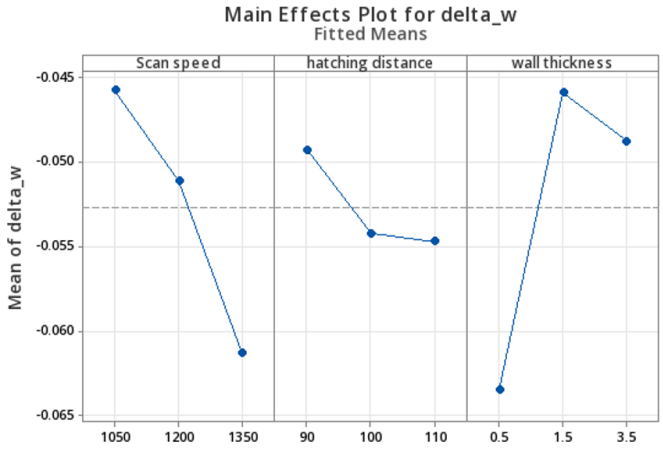

Figure 3.23: Main effects on width (w).

Based on this analysis, the selected parameters are those reported in Table 3.13. This parameter set corresponds to Experiment 5, which featured an intermediate volumetric energy density among the investigated cases.

Table 3.13: Selected process parameters.

Parameter	**Value**
Laser Power	200 W
Scan Speed	1200 mm/s
Hatch Spacing	100 μm

3.5 Job 3: Realization and Characterization of Simplified Springs

After selecting the process parameters, simplified springs with a reduced number of coils were fabricated, with the aim of subsequently characterizing them by calculating the stiffness of the springs and thus identifying the most suitable configuration for the final prototype. In Job 3 three springs were manufactured, each with a coil thickness of 0.5 mm, as defined in the design, while varying the pitch. Specifically, three different pitches were tested: 1.0 mm (the nominal design value), 1.25 mm, and 1.5 mm.

Figure 3.24 shows the outcome of the build. In this case, unlike the previous prints, the upper part of the springs was successfully completed. This improvement can be attributed to the fact that, in Job 2, the coils were tilted with respect to the recoater movement direction, which allowed a more gradual pressure distribution during powder spreading. As can be observed in the image, the springs appear deformed because the cooling rate was too high and the supports were not properly optimized.

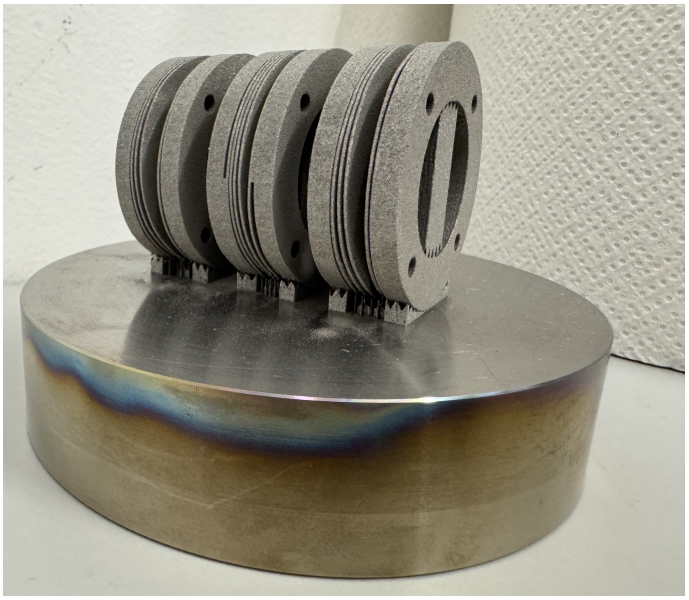

Figure 3.24: Result of Job 3.

3.5.1 Stress Relief Heat Treatment

The heat treatment was carried out at the INRiM laboratory using the furnace shown in Figure 3.25. This specific furnace, manufactured by MB-SAS, has a maximum power of 18 kW and can reach a temperature of up to 1500°C. It provides a usable volume of $200 \times 200 \times 400$ mm^3 and is capable of operating under vacuum conditions, thanks to the pumping system composed of a mechanical pump, a Roots pump, and a cryogenic pump connected in series. This configuration enables the chamber pressure to reach values as low as 10^{-6} mbar.

Figure 3.25: Emmebi furnace.

According to the supplier of the titanium alloy Ti-6Al-4V, the recommended heat treatment consists of holding the material at 920°C for 2 hours. The heating and cooling ramps, as well as the required vacuum level, were defined on the basis of a review of the scientific literature on heat treatments for additively manufactured Ti-6Al-4V [22, 23, 24]. From this analysis, it was concluded that the most effective approach consists in adopting a controlled rate of $5°\mathrm{C\,min^{-1}}$ during both heating and cooling, while maintaining a vacuum level of approximately 10^{-3} mbar.

The complete thermal treatment profile is reported in Figure 3.26.

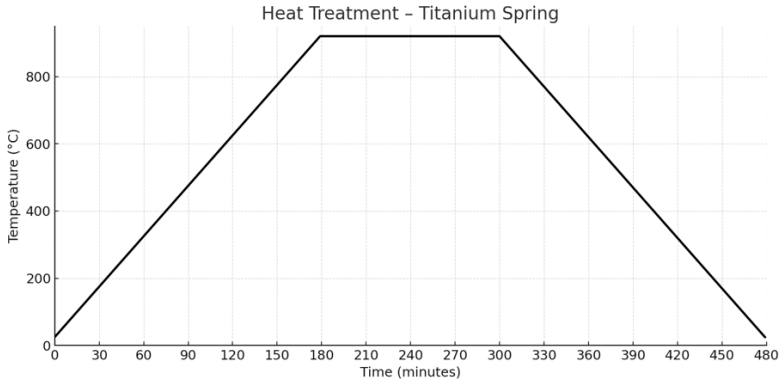

Figure 3.26: Heat treatment cycle.

However, due to technical issues, the heat treatment was not successfully completed, as the target temperature of 920°C could only be maintained for approxi-

mately 10 minutes. Figure 3.27 shows the springs after the heat treatment, highlighting significant distortions.

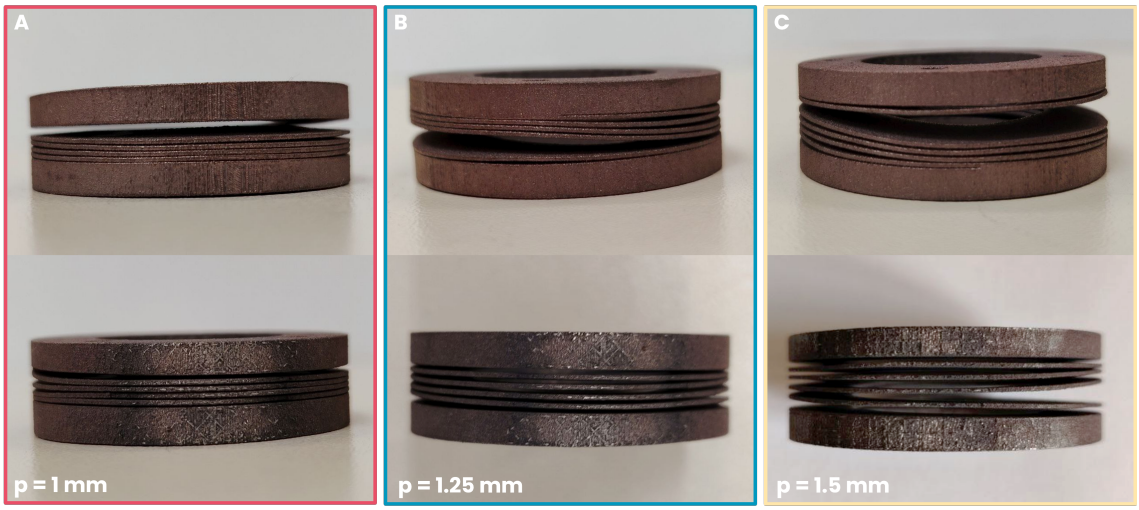

Figure 3.27: Springs of Job 3 after the heat treatment.

After separation from the building platform, the springs were cleaned using an ultrasonic Sonica machine, first with acetone for 5 minutes and subsequently with deionized water for 30 minutes, in order to carefully remove any processing residues, Figure 3.28.

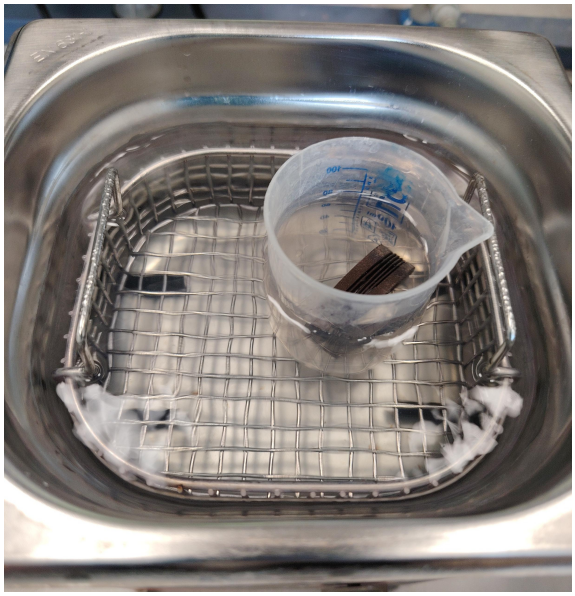

Figure 3.28: Ultrasonic cleaning with a Sonica machine.

3.5.2 Static Analysis

Static tests on the three simplified springs were conducted to calculate their axial stiffness. To this end, known loads were applied using calibrated masses of 11.721g, and the corresponding displacements were measured with the same optical measurement system previously employed, as shown in Figure 3.29. Furthermore, the springs were equipped with a supporting plate to place the masses, as reported in Figure 3.30.

Figure 3.29: Static experimental setup to measure axial stiffness, front view.

Figure 3.30: Static experimental setup to measure axial stiffness, upper view.

The axial stiffness was then obtained as the ratio between force and displacement:

$$k_{\text{axial}} = \frac{F}{\Delta x}$$

where F is the applied force, computed as $F = m \cdot g$, with m the applied mass and g the gravitational acceleration, and Δx is the measured displacement.

In Figures 3.31, 3.32a, and 3.32b, the force–displacement diagrams of the three springs are shown. The stiffness remains nearly constant up to displacements of approximately 4 mm, while at higher displacements it exhibits a slight increase. No substantial differences emerge among the springs with different pitches, indicating no particular advantage in using larger pitches: the spring with a 1.00 mm pitch exhibits an axial stiffness of 0.119 ± 0.001 N/mm, the 1.25 mm pitch 0.121 ± 0.001 N/mm, and the 1.50 mm pitch 0.122 ± 0.002 N/mm. These stiffness values were obtained by performing a linear regression on the first five data points shown in the figures.

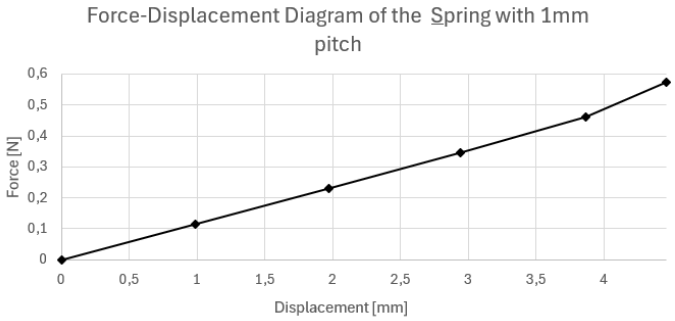

Figure 3.31: Force–displacement diagram, 1 mm pitch.

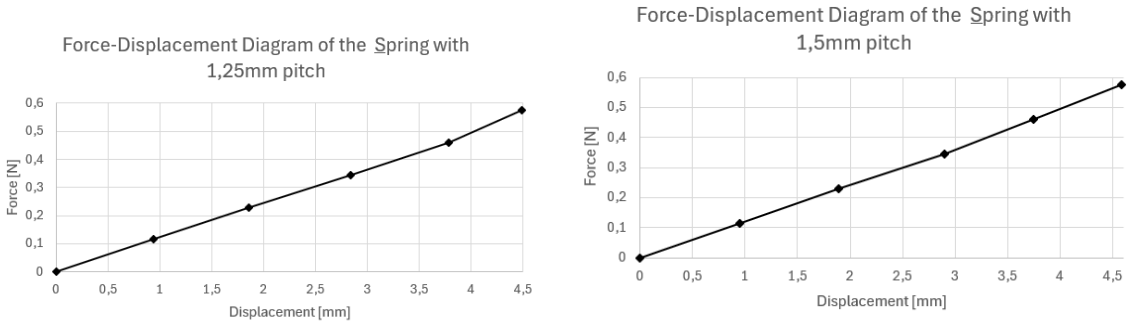

a) b)

Figure 3.32: a) Force–displacement diagram, 1.25 mm pitch; b) Force–displacement diagram, 1.5 mm pitch.

3.5.3 Dynamic Analysis

A dynamic analysis was also carried out on one of the three manufactured springs, specifically the one with a pitch of 1 mm, corresponding to the nominal dimensions defined in the initial specifications. Axial and transverse oscillations were measured in the same way as for the aluminum alloy spring. The corresponding PSDs were then computed, revealing identical natural frequencies due to the coupled modes, as already observed in the preliminary spring study.

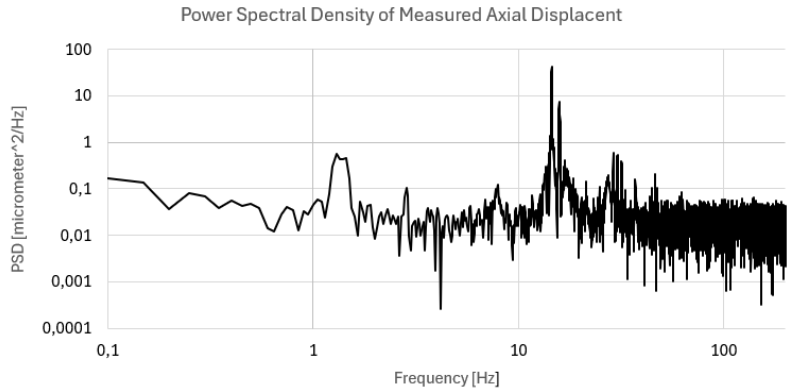

Figure 3.33: PSD of the axial displacement of the 1 mm pitch spring.

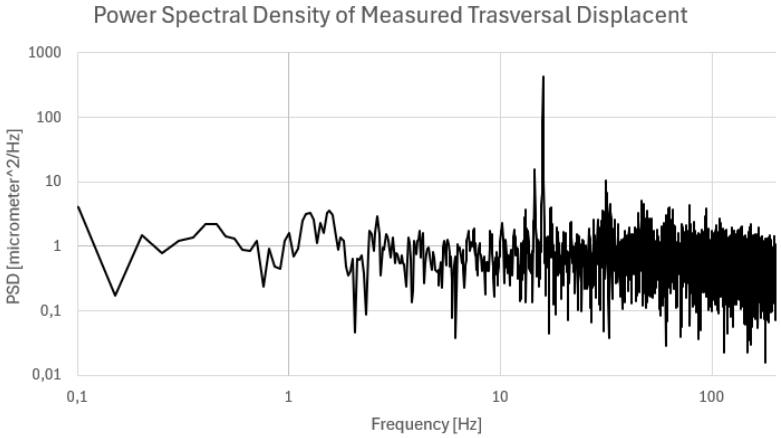

Figure 3.34: PSD of the transverse displacement of the 1 mm pitch spring.

In Figures 3.33 and 3.34, the PSDs of the measured axial and transverse displacements are reported. These analyses highlighted the following natural frequencies, summarized in Table 3.14.

Table 3.14: Natural frequencies of the simplified spring with 1 mm pitch.

Mode	**Frequency [Hz]**
1^{st} axial frequency	14.49
1^{st} transverse frequency	15.77
2^{nd} transverse frequency	15.90

Subsequently, a finite element simulation was carried out to evaluate the first three natural frequencies. As shown in Figure 3.35, they converge to 15.90 Hz, 17.46 Hz, and 17.56 Hz, respectively.

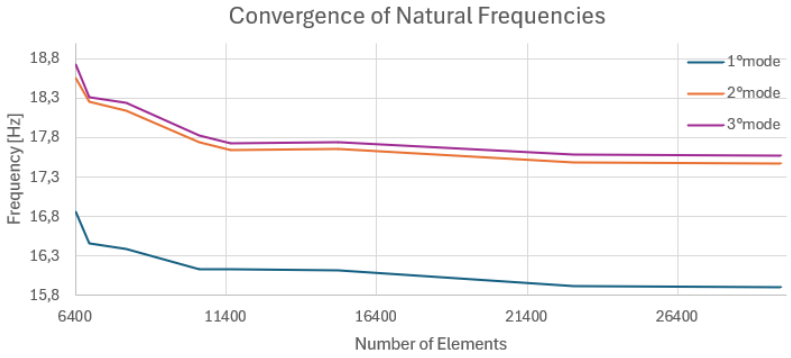

Figure 3.35: Convergence of the first three natural frequencies of the 1 mm pitch Ti6Al4V spring.

By comparing the results obtained from the analysis, the FEM simulation, and the experimental measurements, it can be observed that the measured frequencies are lower than the simulated ones, similarly to the case of the AlSi10Mg spring. This indicates a higher stiffness in the finite element model, a typical phenomenon in such simulations. Since the deviation between the experimental and simulated values remains approximately 10% in all analyzed cases, the results can be considered acceptable, and the springs perform even better than initially expected, while still meeting the requirement of achieving as low bending natural frequencies as possible.

The comparison is reported in Table 3.15.

Table 3.15: Comparison between experimental and FEM natural frequencies of the 1 mm pitch spring.

Mode	**Experimental [Hz]**	**FEM [Hz]**	**Deviation [%]**
1^{st} axial natural frequency	14.49	15.90	9.7
1^{st} transverse natural frequency	15.77	17.46	10.8
2^{nd} transverse natural frequency	15.90	17.56	10.5

3.6 Job 4: Final Prototype

Following the study on simplified springs, no substantial differences in axial stiffness were observed when varying the pitch from the originally designed value of 1.00 mm. Accordingly, the final prototype was manufactured with a 1.00 mm pitch and the same optimized process parameters that are summarized in Table 3.16.

Table 3.16: Process parameters for the final prototype.

Parameter	**Value**
P	200 W
v	1200 mm/s
h	100 μm

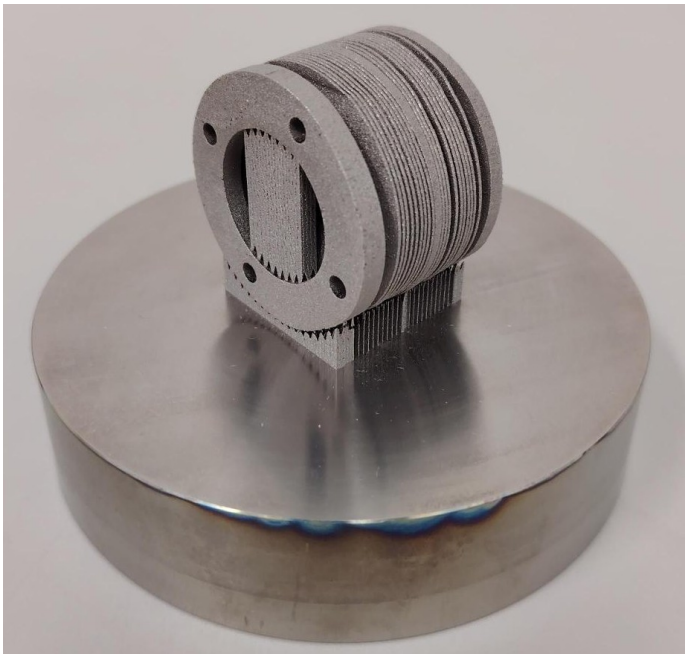

Figure 3.36: Final prototype.

As Figure 3.36 shows, distortions on the spires are present in the final prototype, caused by issues with the production of supports. This indicates that there is still room for improvement by optimizing the supports. However, for the purpose of the

microgravity qualification experiment, the prototype can be considered acceptable as long as the natural frequencies meet the required specifications. In order to prevent additional distortions caused by residual stresses, the same post-processing sequence as previously adopted was applied. Specifically, a heat treatment was performed with heating and cooling rates of 5 °C/min up to 890 °C, followed by a 2 h hold at 890 °C (Figure 3.37). The target temperature was reduced with respect to the previous heat treatment to increase the stability of the furnace and avoid further malfunctions.

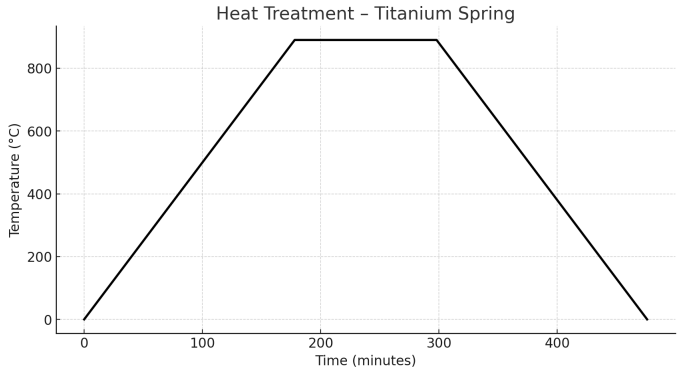

Figure 3.37: Heat treatment cycle for final prototype.

The prototype was then removed from the build plate, the internal supports were removed, and the part was cleaned in an ultrasonic bath before proceeding with static and dynamic testing,as done in Job 3.

3.6.1 Static Analysis

A static analysis—analogous to that performed in Job 3—was carried out by applying a known mass of 11.721 g and measuring the resulting displacement. The axial stiffness was obtained via a linear regression of the three measured points, as shown in Figure 3.38. The resulting axial stiffness is 0.0254 ± 0.0002 N/mm.

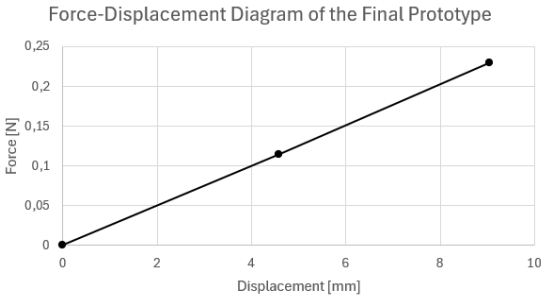

Figure 3.38: Force–displacement curve of the final prototype.

As expected, when comparing the axial stiffness of the final prototype with that of the simplified spring with a 1 mm pitch from Job 3, the stiffness is lower for the final prototype (Table 3.17), as it features a greater number of coils.

Table 3.17: Axial stiffness comparison between the simplified spring (1 mm pitch) and the final prototype.

	Axial Stiffness [N/mm]
1 mm pitch spring (Job 3)	0.119 ± 0.001
Final Prototype	0.0254 ± 0.0002

3.6.2 Dynamic Analysis

A dynamic analysis was performed, as previously done, to determine the natural frequencies and to qualitatively estimate the damping ratio and time constant of the final prototype. The tests were conducted using both a transverse experimental setup (Figure 3.39a) and an axial experimental setup (Figure 3.39b).

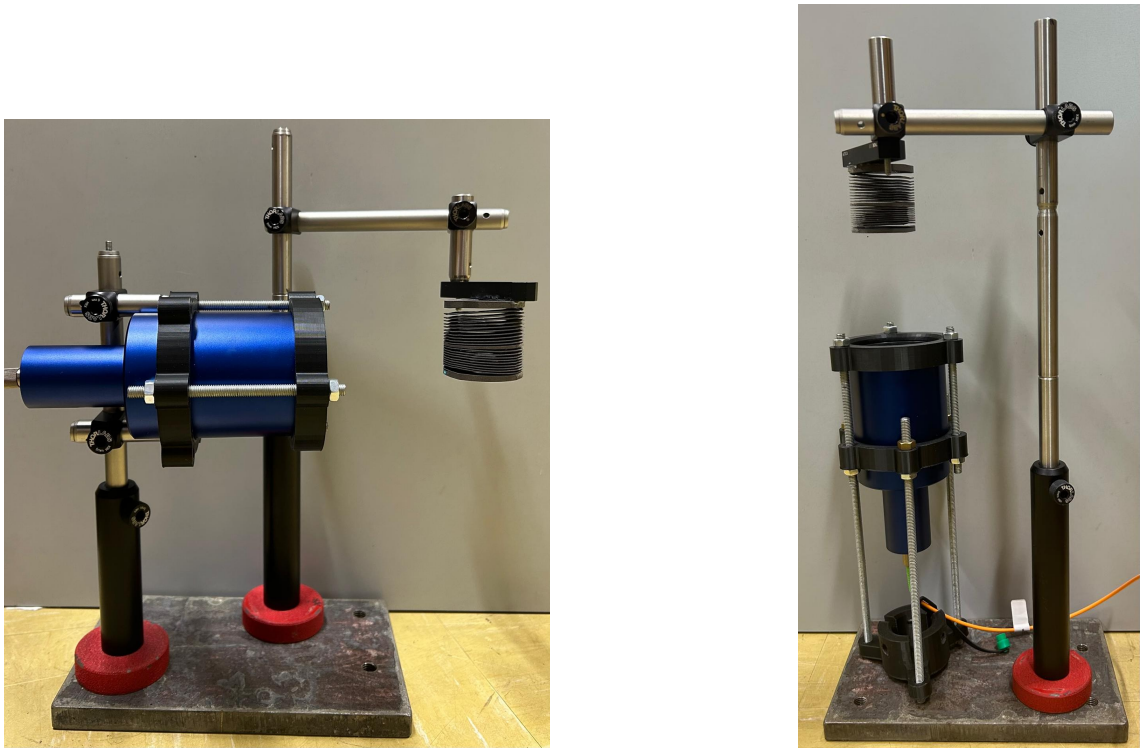

a) b)

Figure 3.39: a)Transverse experimental setup; b) Axial experimental setup.

As expected, coupled vibration modes were also observed in the final prototype. This behavior is evident from the time history of the transverse displacements shown in Figure 3.40, where a beating pattern can be clearly identified.

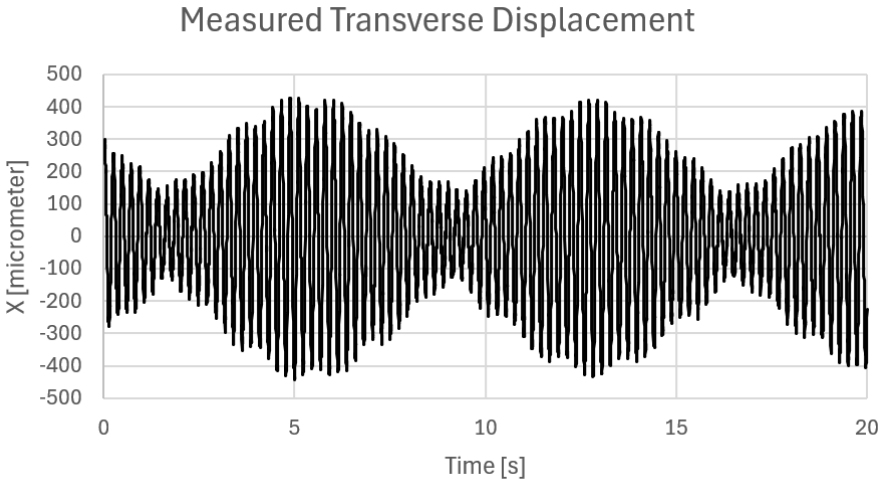

Figure 3.40: Time history of measured transverse displacement.

Subsequently, the PSD of the displacement signal was computed to identify the natural frequencies. In the double–logarithmic plot, Figure 3.41 reports the PSD of the transverse displacements, while Figure 3.42 shows the PSD of the axial displacements. Three dominant peaks are evident: two close to 4.34 Hz and 4.50 Hz—responsible for the beating observed in the previous figure and associated with the two bending modes—and a third peak at 5.10 Hz, corresponding to the first axial mode.

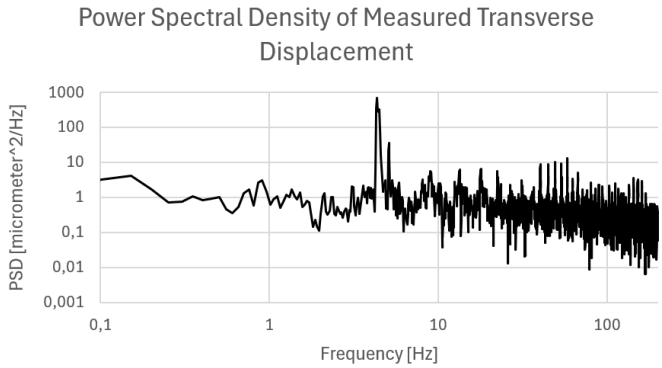

Figure 3.41: PSD of the transverse displacement.

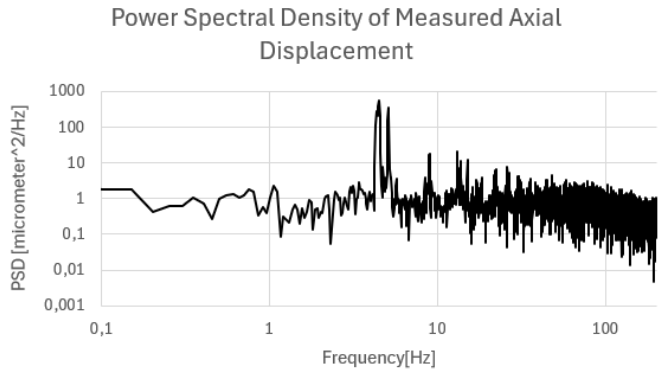

Figure 3.42: PSD of the axial displacement.

To obtain a qualitative estimate of the damping ratio and the time constant, we adopted the same approach as in Job 1: ζ and τ were computed via the logarithmic-decrement method, assuming that the two bending natural frequencies responsible for the beating effect were ideally coincident. Three pairs of peaks were considered,

and the resulting values were then averaged. Figures 3.43a and 3.43b show the peaks selected for the estimation of the transverse and axial ζ_{avg} and τ_{avg} respectively. The results of this estimation are reported in Table 3.18.

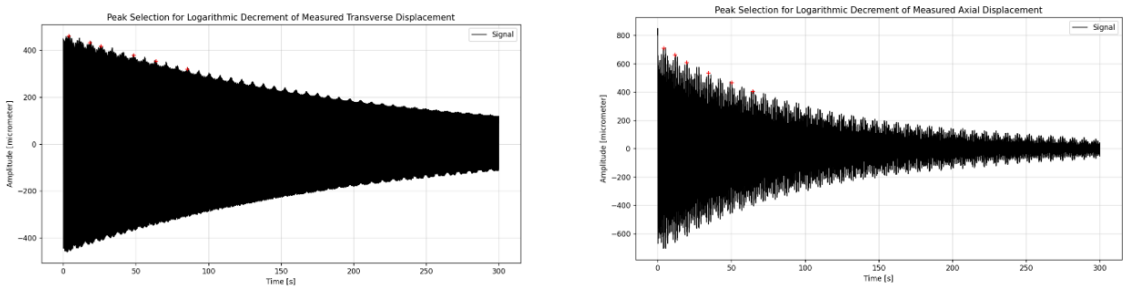

a) b)

Figure 3.43: Peaks used to estimate the transverse (a) and axial (b) damping ratio and time constant.

Table 3.18: Average results of the damping ratio ζ and the time constant τ for the final prototype.

Parameter	**Transverse oscillations**	**Axial oscillations**	**Unit**
τ_{avg}	$\sim 10^3$	$\sim 10^3$	s
ζ_{avg}	$\sim 10^{-4}$	$\sim 10^{-4}$	–

Afterwards, a finite element simulation was performed to assess the convergence of the first three natural frequencies, following the same procedure adopted previously. The converged eigenfrequencies are 4.68 Hz, 4.69 Hz, and 5.60 Hz, respectively (Figure 3.44).

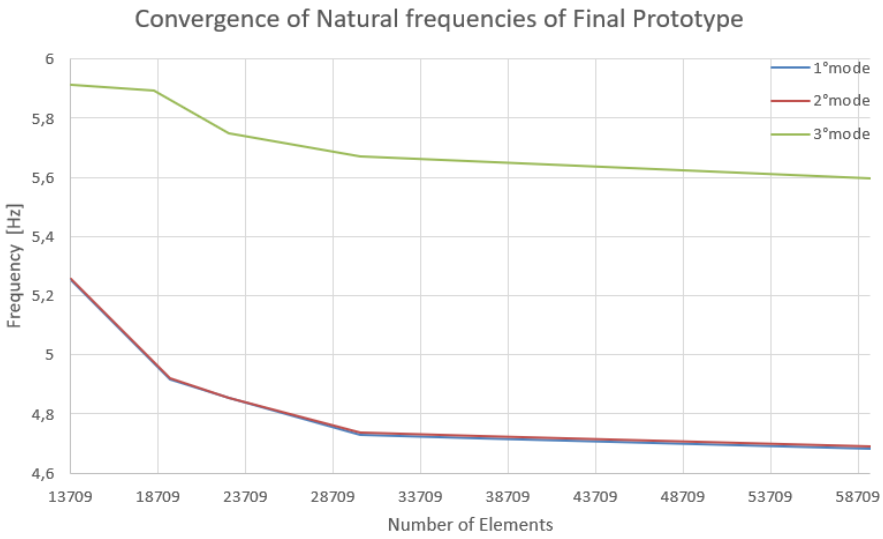

Figure 3.44: Convergence of natural frequencies of the final prototype

By comparing the measured natural frequencies with the FEM simulations, it was observed—consistently with previous cases—that the measured values are lower than the simulated ones. In this instance the discrepancy is even smaller than Job 3: it remains below 8% for the bending modes and reaches about 9.7% for the axial mode. The comparison is summarized in Table 3.19.

Table 3.19: Comparison between experimental and FEM natural frequencies of the final prototype.

Mode	**Experimental [Hz]**	**FEM [Hz]**	**Deviation [%]**
1st transverse natural frequency	4.34	4.68	7.9
2nd transverse natural frequency	4.50	4.69	4.3
1st axial natural frequency	5.10	5.60	9.7

Therefore, the spring behaves as expected, and the initial specification—namely, achieving bending natural frequencies of the mass–spring system below 1 Hz—can be considered met once the mass is added, with the combined system reaching approximately 0.46 Hz. Moreover, the spring exhibits a sufficiently low damping ratio,

ensuring that quasi-static accelerations during in-space operation are not excessively attenuated and contributing to the reduction of both thermal and mechanical noise.

Test Bench Preparation for Zero Gravity Tests

In this chapter, the preparation of the test bench for performing zero-gravity experiments at the Einstein Elevator facility of the Hannover Institute of Technology, Leibniz University of Hannover, is presented. The objective of the experiment is to verify the dynamic behavior of the mass–spring system by comparing it with the theoretical model through the acquisition of the displacement of eight markers on the proof mass — four on one face and four on the opposite as shown in Figure 4.1 — in order to monitor all six degrees of freedom of the rigid body, as required by ESA.

To achieve this, the test bench (Figure 4.1) was equipped with two cameras dedicated to the measurement of the marker displacements and two additional cameras for monitoring the experiment. The latter provide visual verification of the actual motion of the mass, serve to validate the acquired data, and represent a useful support in case of malfunctions or anomalies during acquisition. Furthermore, the setup includes sensors to validate the experimental conditions, such as pressure, temperature, and acceleration, as well as dedicated systems for power supply and illumination.

The chapter begins by presenting the main components, with particular attention to the MEMS accelerometer GY-521, for which an additional study on characterization and dynamic calibration was carried out and to the acquisition system of the sensors managed by a microcontroller. Subsequently, the acquisition system for

tracking the displacement of the markers on the proof mass and the video acquisition system of the monitoring cameras are described.

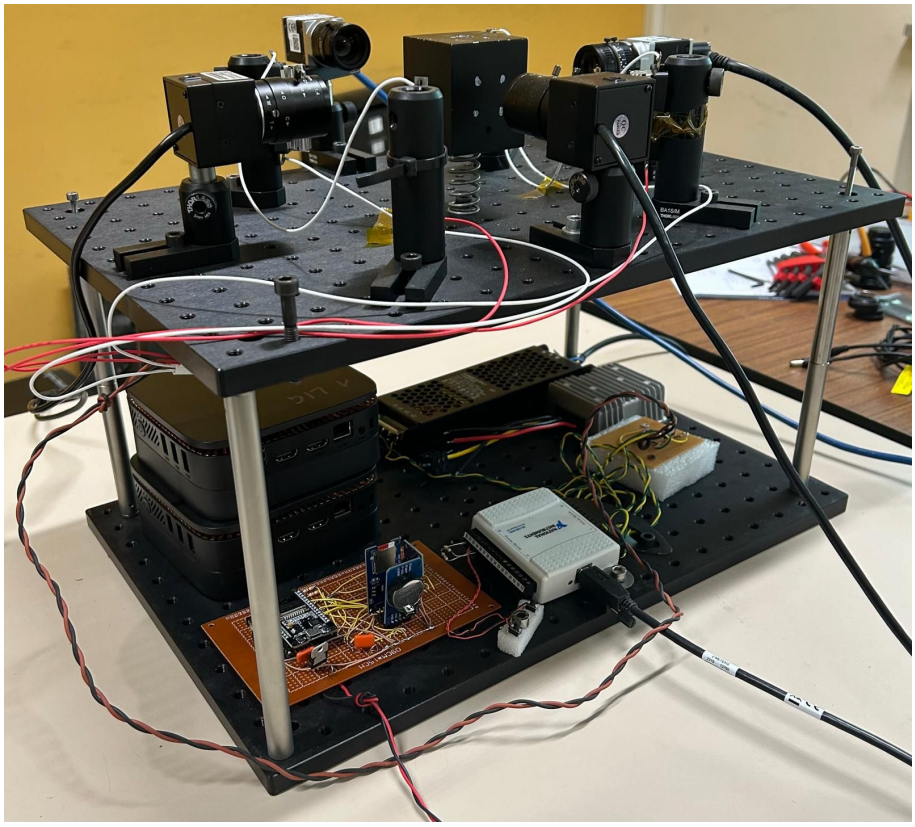

Figure 4.1: Test Bench.

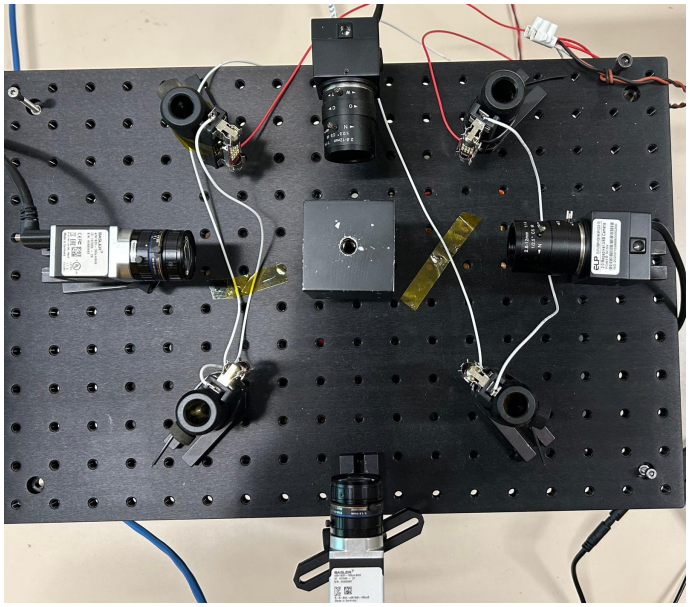

Figure 4.2: Test bench,upper view.

4.1 Hardware Assembly Components

4.1.1 Test Bench Cameras

The experimental setup included two types of cameras: Basler ace 2 Basic cameras (figure 4.3a) for marker detection, and Svpro 8MP webcams (Figure 4.3b) for full-scene video recording.

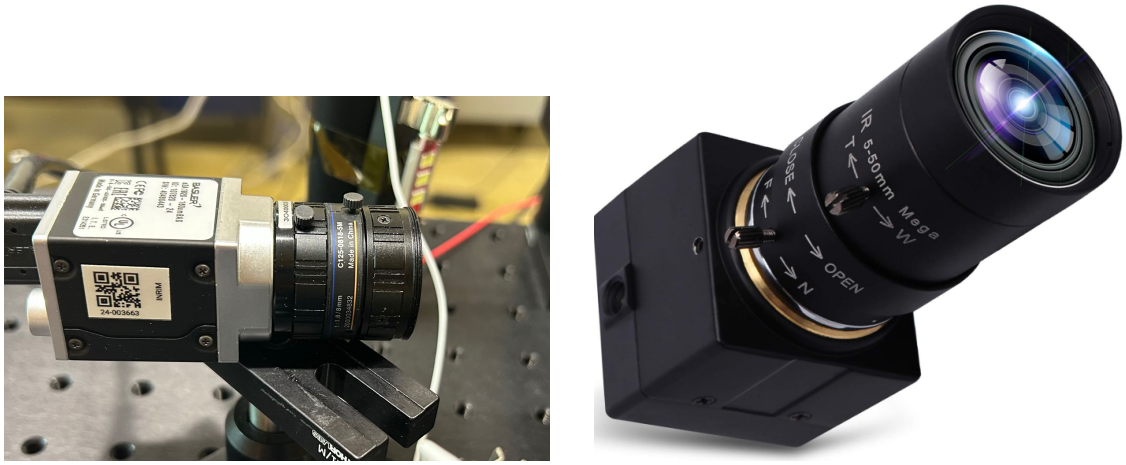

a) b)

Figure 4.3: a) Basler ace 2 Basic and Basler C125-0818-5M-P lens; b) Svpro 8MP camera.

The Basler ace 2 Basic – model a2A1920-160umBAS – industrial cameras were used for the acquisition of the markers during the tests. These cameras enable high-speed and distortion-free acquisition, which is essential for the accurate tracking of the markers during the vibration of the mass-spring system, thanks to the direct acquisition of the region of interest (ROI) . Their compact size and USB 3.0 connectivity facilitate easy integration into the experimental setup, especially within the LabVIEW environment.

Although the datasheet of the Basler C125-0818-5M-P lens (Table 4.1 and Table 4.2) specifies a nominal minimum focus distance of about 10 cm, in practice it was

observed that sharp focus can also be achieved at shorter distances (approximately 5 cm) by manually adjusting the optics. This allowed the cameras to be positioned closer to the sample, optimizing the framing and resolution of the markers.

Table 4.1: Technical specifications of the Basler ace 2 Basic camera.

Parameter	**Value**
Camera model	Basler ace 2 Basic – a2A1920-160umBAS
Resolution	1920 × 1200 px (approx. 2.3 MP)
Maximum framerate	160 fps
Dimensions	42.8 × 29 × 29 mm^3
Interface	USB 3.0
Features	External trigger compatibility, synchronous acquisition

Table 4.2: Technical specifications of the Basler C125-0818-5M-P lens.

Parameter	**Value**
Lens model	Basler C125-0818-5M-P
Focal length	8 mm
Nominal minimum focus distance	10 cm
Observed focus distance	approx. 5 cm (manual adjustment)
Optical resolution	230 LP/mm (2.2 µm pixel size)

In addition to the Basler cameras, two Svpro USB webcams were used for video recording of the experiment. These devices are equipped with a 5–50 mm zoom lens and manual focus, allowing flexible adjustment of the field of view and depth of field. Their high image resolution ensures high-quality footage of the overall test environment.

Table 4.3: Technical specifications of the Svpro USB webcam.

Parameter	**Value**
Camera model	Svpro USB Webcam
Resolution	3264 × 2448 px (8 MP)
Focus	Manual
Lens type	Zoom 5–50 mm
Dimensions	39 × 39 × 75 mm^3
Purpose	Full-scene video recording

4.1.2 LEDs

The test bench was also equipped with four LED modules, each consisting of 12 LEDs arranged along a 41 mm strip, as shown in Figure 4.4. These modules are powered at 12 V and are particularly well-suited for this application due to their compatibility with the National Instruments data acquisition system, which allows for robust and efficient control.

Figure 4.4: BDX53C LED module.

As Figure 4.5 shows, the electronic circuit to switch on the LED was also equipped with a diode to block reverse currents that could potentially damage the circuit. Although LEDs are not inherently inductive loads, this protective feature

is still beneficial, especially when long cables or electromagnetic interference could cause voltage spikes or transients.

As the available power supply operates at 24 V, the LED modules were wired in pairs, with two modules connected in series per branch and each pair wired in parallel. This configuration ensures correct voltage distribution and reliable operation across all modules.

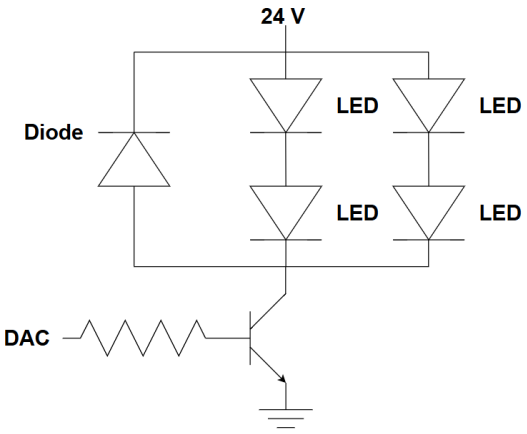

Figure 4.5: Electronic circuit of the BDX53C transistor.

4.1.3 Sensors and Microcontroller

Although the *Einstein Elevator* already provides access to various environmental monitoring sensors—such as temperature, pressure, relative humidity, and additional accelerometers—to ensure proper control of the experimental conditions, we further equipped the test bench with additional electronic sensors managed by an ESP32 microcontroller (Figure 4.6a) that can operate independently from the minipcs. Among these, a BMP085 sensor (Figure 4.6b) was used to monitor ambient pressure and temperature, and a GY-521 MEMS accelerometer (Figure 4.6c) to collect acceleration data. The setup also included a microSD adapter for data storage, a battery-powered real-time clock (Figure 4.6d) to timestamp the acquisitions, and a button to reset the SD if necessary.

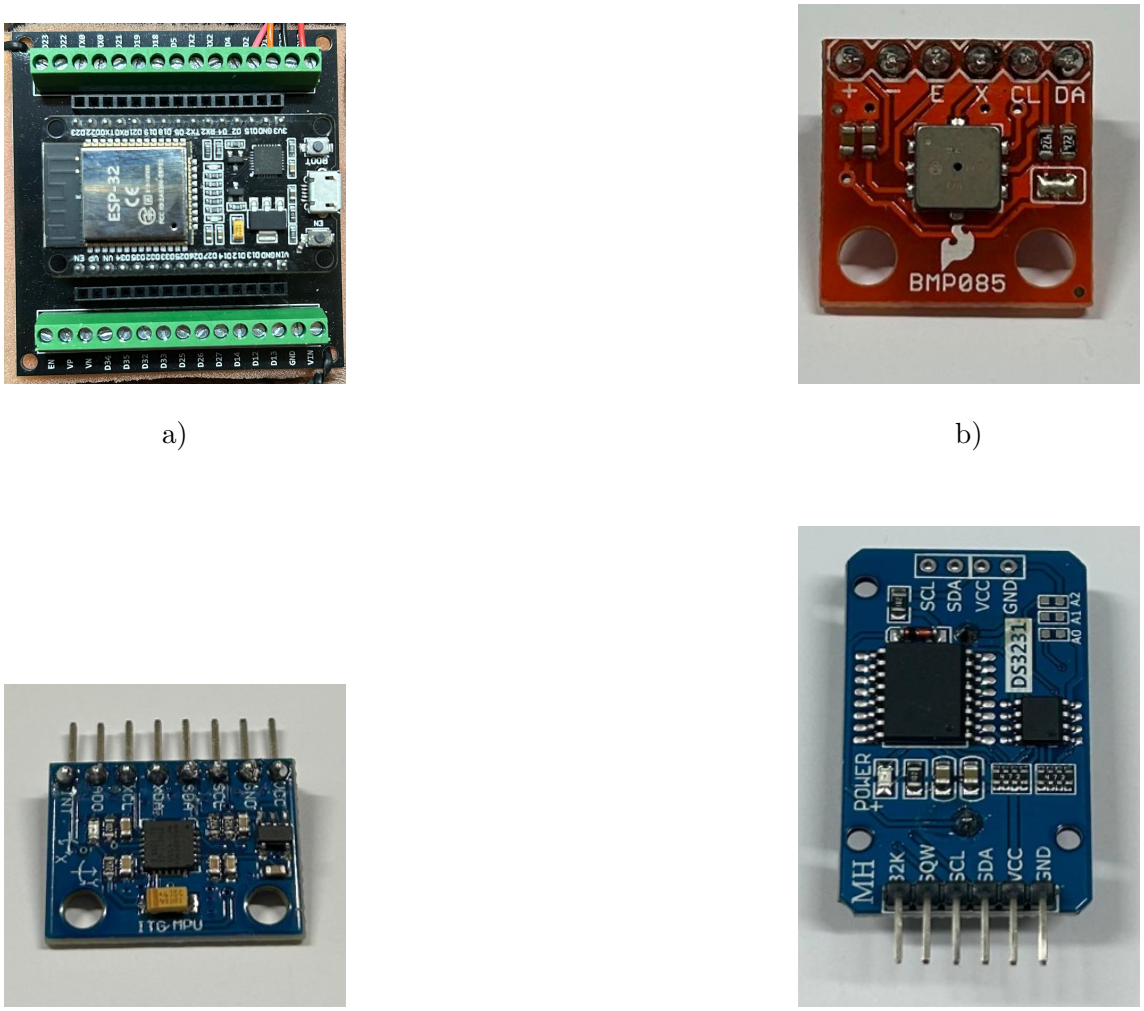

a) b)

c) d)

Figure 4.6: a) ESP32 microcontroller; b) BMP085 pressure and temperature sensor; c) GY-521 MEMS accelerometer; d) RTC DS3231.

A firmware in C/C++ (Arduino Core) was developed for the ESP32 to acquire: (i) accelerations via the GY-521 (MPU6050) module at 200 Hz, (ii) pressure and temperature via the BMP085 at 5 Hz, (iii) absolute timestamp via DS3231 RTC that provides a 1 Hz time reference. Data are written when available with the following structure:

```
YYYY-MM-DD hh:mm:ss, acc_x, acc_y, acc_z, pressure, temperature
```

where the units are: acc_x, acc_y, acc_z in m/s^2, pressure in Pa, temperature in

°C. The data are then saved to a microSD in CSV format, making acquisition independent of external mini-PCs and preserving timestamps useful for comparison with experimental data from launches in the Einstein Elevator.

The architecture adopts a concurrent model based on FreeRTOS, a lightweight real-time operating system that provides prioritized tasks and synchronization primitives. In particular, independent tasks are defined for: (i) accelerometer and timestamp acquisition, (ii) pressure and temperature acquisition , and (iii) SD writing. Access to the I2C bus is serialized through a mutex , ensuring exclusive use of the shared resource during each transaction.

The I2C lines are equipped with physical 3.9 kΩ pull-up resistors to ensure adequate rise times and greater stability compared to relying solely on the internal pull-ups of the modules.

To decouple time-critical acquisition from SD I/O, which has variable latency, a queue residing in the ESP32's internal RAM is employed, consisting of 300 elements of 160 B each (about 48 kB total). The SD task drains the queue in the background, writing one CSV row per sample; an explicit flush to the SD is performed every 200 rows . If the queue saturates, a drop-oldest policy is applied, which means that the oldest row is discarded, preventing acquisition stalls. Long-duration tests indicate that, under the intended operating conditions, queue saturation does not occur.

Figure 4.7 shows the hardware architecture used for data acquisition. The system is equipped with a voltage regulator 7805 that steps down the 12 V supplied by the transformer to the 5 V required to power the ESP32, along with two decoupling capacitors to stabilize the 5 V and 3.3 V rails.

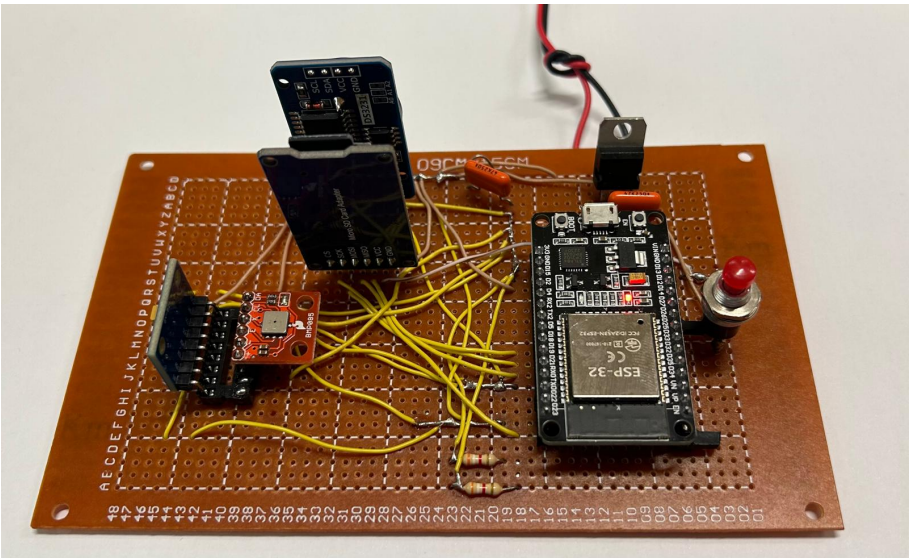

Figure 4.7: Hardware architecture employed for acquisition.

Since acceleration was the main parameter of interest, the MEMS sensor was first characterized for noise under static conditions and then calibrated through dynamic testing.

To characterize the MEMS accelerometer, three static tests were performed by changing the sensor orientation so that, in each configuration, one axis was aligned with the gravity vector. During the measurements, the sensor was kept stationary on the floor to avoid any perturbations and to acquire only external noise. The instrumental noise level was estimated by analyzing the standard deviation of the measured signal on each axis, expressed in $\mathrm{m/s^2}$.

The accelerometer outputs its measurements in digital counts (LSB), representing the raw sensor data. For the selected sensitivity of $\pm 2\,g$, the full-scale range corresponds to 16384 LSB per g, as the sensor is 16-bit. To convert the raw output into physical units of acceleration, the counts were multiplied by a factor of $9.81/16384$ $\mathrm{m/s^2}$ per LSB. This conversion allows the acceleration along each axis to be expressed directly in $\mathrm{m/s^2}$.

The data acquisition was carried out at a sampling frequency of 200 Hz for a duration of one hour, providing a sufficiently long dataset to estimate the noise

characteristics while averaging out the effect of random external disturbances.

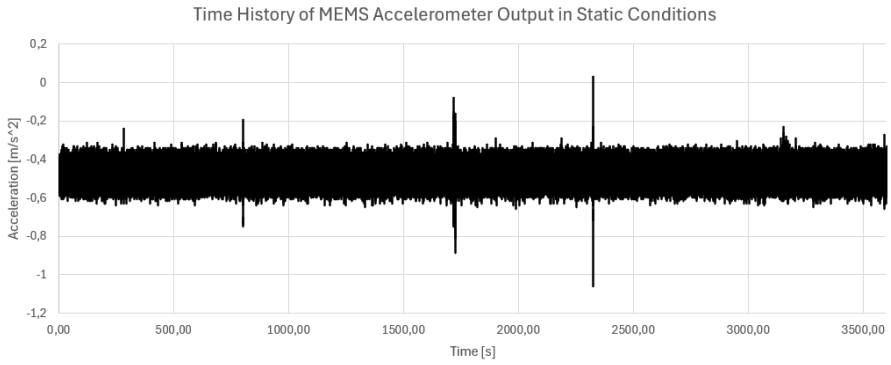

Figure 4.8: Time history of the x-axis output of the MEMS accelerometer in static conditions.

Figure 4.8 shows the time history of the x-axis output of the MEMS accelerometer, with the y-axis aligned with the gravity vector in static conditions . It can be observed that some external disturbances increase the amplitude of the measured acceleration. Moreover, the mean value is slightly negative, which can be attributed to a small misalignment of the sensor axis with respect to the horizontal plane, but for the purpose of this test it is not influential.

Table 4.4: Standard deviation of the measured acceleration along each axis for different sensor orientations.

Axis aligned with gravity vector	σ_x $[\mathbf{m/s^2}]$	σ_y $[\mathbf{m/s^2}]$	σ_z $[\mathbf{m/s^2}]$
X	3.52E-02	3.25E-02	5.37E-02
Y	4.06E-02	3.41E-02	7.35E-02
Z	4.29E-02	3.34E-02	8.49E-02

From the analysis of the standard deviations measured along the three axes in the different sensor orientations, it can be observed that the noise levels are overall comparable, with variations of roughly half an order of magnitude, ranging from about $0.034\,\mathrm{m/s^2}$ to $0.085\,\mathrm{m/s^2}$. Among the three axes, the Z axis exhibits slightly

higher noise, reaching a maximum value of approximately $0.085\,\mathrm{m/s^2}$.

No systematic correlation was observed between the axis aligned with the gravity vector and an increase in noise. This indicates that the contribution of the gravity-induced signal does not significantly affect the variance, and the standard deviation can therefore be considered a robust estimate of the instrumental noise under static conditions.

After characterizing the noise of the GY-521 sensor under static conditions, a dynamic calibration phase was carried out. The MEMS sensor, together with a piezoelectric accelerometer, was mounted on a vibration generator capable of producing a controlled sinusoidal excitation. During the test, the accelerations measured by the GY-521 and by the reference piezoelectric sensor were acquired simultaneously, while the vibration frequency was progressively varied.

The purpose of the calibration was to compare the RMS accelerations measured by the two devices, in order to evaluate the accuracy and the frequency response of the GY-521 with respect to a higher-class metrological sensor.

This analysis phase allows the identification of the operational limits of the MEMS sensor and the assessment of its suitability for dynamic measurements within the desired frequency ranges.

The reference sensor used for the dynamic calibration is the PCB Piezotronics 532C33, shown in Figure 4.9.

Figure 4.9: PCB Piezotronics 532C33 reference accelerometer.

Table 4.5: Main specifications of the reference piezoelectric accelerometer PCB Piezotronics 532C33.

Property	**Value**
Sensitivity at 100 Hz	98.6 mV/g $\approx$ 10.05 mV/(m/s^2)
Resonance frequency	51.2 kHz
Measurement range	$\pm$50 g
Resolution (RMS)	0.00015 g
Spectral noise density @ 1 Hz	39 μg/$\sqrt{\text{Hz}}$ $\approx$ 0.000382 m/s^2/$\sqrt{\text{Hz}}$

As reported in Table 4.5, this device features a very high resonance frequency (51.2 kHz) and a wide measurement range of $\pm$50 g, making it suitable for dynamic tests without saturation even in the presence of strong vibrations. Its high sensitivity (98.6 mV/g) and extremely low noise floor (39 μg/$\sqrt{\text{Hz}}$) ensure precise detection of small accelerations, providing a reliable benchmark for evaluating the performance of the MEMS accelerometer.

These characteristics ensure that the reference sensor introduces negligible errors in the frequency band of interest, allowing an accurate and precise assessment of the dynamic behavior of the MEMS accelerometer.

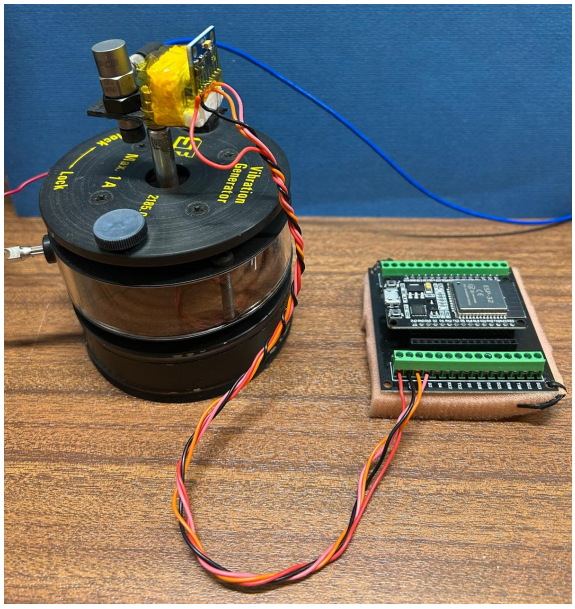

Figure 4.10: Dynamic calibration setup: vibration generator.

The comparison between the two sensors was carried out by analyzing the RMS value of the sinusoidal signal produced by the vibration generator at different excitation frequencies, as shown in Figure 4.10, and subsequently comparing the results of the two devices. Tests were performed in three different configurations by varying the orientation of the MEMS sensor so that only one axis was sensitive to gravity at a time. To ensure data comparability, the static bias due to gravitational acceleration was removed from the MEMS signal, allowing the calculation of a centered RMS value.

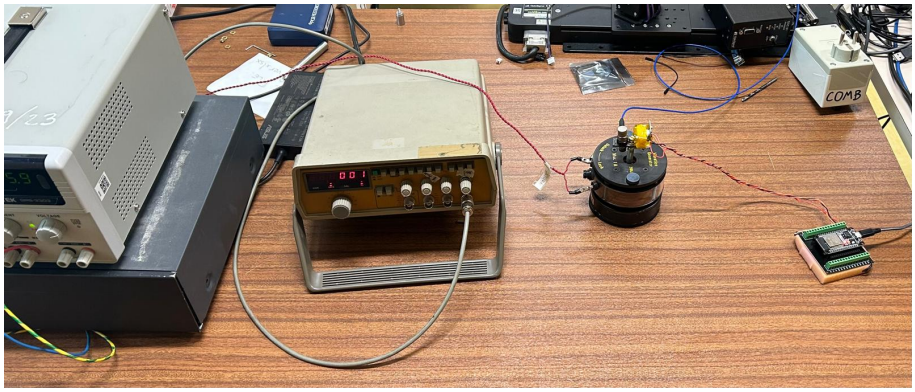

Figure 4.11: Dynamic calibration setup: complete system including vibration generator and amplifier.

During the dynamic calibration, the MEMS accelerometer was configured with a sensitivity of $\pm 8\,g$, which corresponds to a conversion factor of $9.81/4096\,\mathrm{m/s^2}$ per LSB. The MEMS sensor acquired data at a sampling frequency of 1 kHz, whereas the reference piezoelectric accelerometer was sampled at either 1 kHz or 10 kHz, depending on the excitation frequency of the vibration generator. This setup ensured that both sensors captured the dynamic response accurately over the entire frequency range of interest.

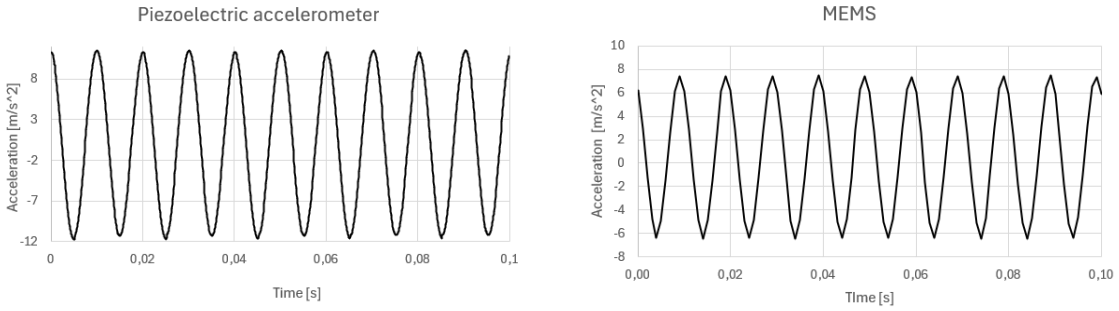

a) b)

Figure 4.12: Time history of the Y-axis acceleration measured by the piezoelectric accelerometer (a) and the MEMS accelerometer (b) under 100 Hz sinusoidal excitation;

Figure 4.12a and Figure 4.12b show the time histories of the Y-axis acceleration

measured by the two sensors during the dynamic calibration test. The piezoelectric accelerometer provides the reference signal, while the MEMS accelerometer captures the corresponding response. This direct comparison highlights the different amplitude levels and the higher noise present in the MEMS measurement.

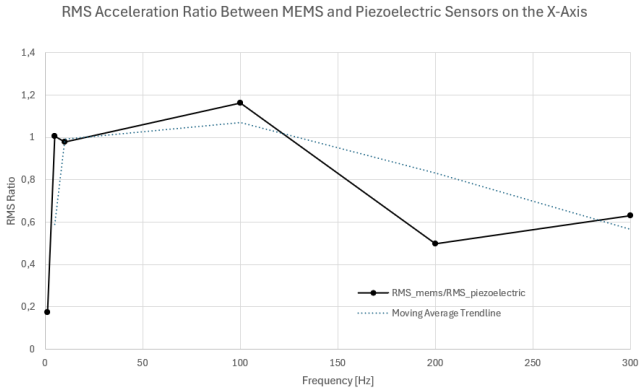

Figure 4.13: RMS ratio between the MEMS and the piezoelectric accelerometer along the X-axis.

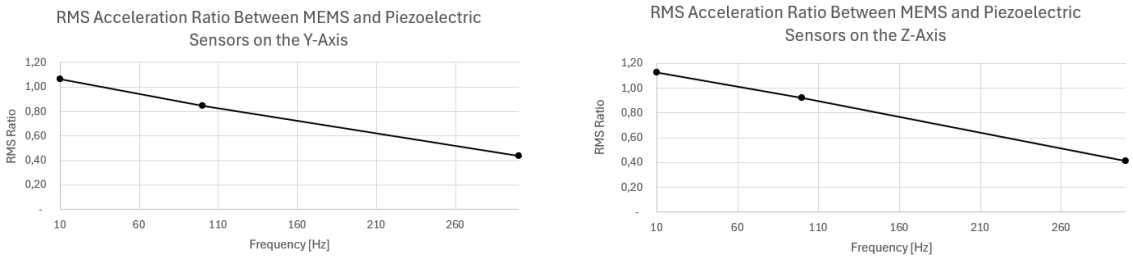

a) b)

Figure 4.14: RMS ratio between the MEMS and the piezoelectric accelerometer along the Y-axis (a) and Z-axis (b)

The Figures above (Figures 4.14,4.14a, 4.14b) show the ratios between the RMS acceleration measured by the MEMS sensor and that measured by the piezoelectric reference sensor along the three axes. The tests were performed with the sensor oriented in three configurations, so that the X, Y, and Z axes were sequentially aligned with the gravity vector.

For the Y- and Z-axis measurements (Figures 4.14b and 4.14c), three discrete excitation frequencies were tested,approximately 10, 100, and 300 Hz, while for the X-axis (Figure 4.13) a finer frequency sweep was conducted to obtain a smoother and more continuous curve. To improve the readability of the experimental trend, a moving average was applied to the measured RMS values.

As can be observed, the relative amplitude starts to decay from approximately 100–150 Hz, which is consistent with the expected behavior of the MEMS sensor. This attenuation is mainly due to the internal digital low-pass filter (DLPF), configured with a cut-off frequency of 260 Hz, which leads to a progressive reduction of the amplitude at higher frequencies.

4.1.4 Power Supply

A DT-NT24V-300W power supply was employed in the test bench to simulate the power source that will later be available from the Einstein Elevator Facility. Consequently, this component will not be included in the actual experimental tests. The unit has a rated power of 300 W, delivers a maximum current of 12.5 A, and provides a constant 24 V DC output. This specific model was selected for its stability and low-noise operation, as well as its aluminum housing with ventilation slots that enhance heat dissipation, ensuring excellent performance. An image of the power supply used is shown in Figure 4.15.

Figure 4.15: DT-NT24V-300W power supply.

4.1.5 Transformer

For the test bench, a transformer is required; in this case, the XW-24-12-120W model from XWST was adopted. This device is a DC-DC converter that steps down from 24 V DC to 12 V DC, enabling the system to operate with both 24 V and 12 V supplies. Specifically, the 24 V line powers the LEDs, while the 12 V line supplies the mini PCs. This converter supports a wide input voltage range, from 18 V to 28 V, making it fully compatible with the 24 V input provided by the Einstein Elevator Facility. It also ensures high performance, with an efficiency greater than 93%, which reduces both power consumption and self-heating. Furthermore, it features a protective coating that safeguards the unit against shocks and possible water exposure. In addition, it is equipped with overcurrent, overtemperature, and short-circuit protection. Figure 4.16 shows the converter adopted.

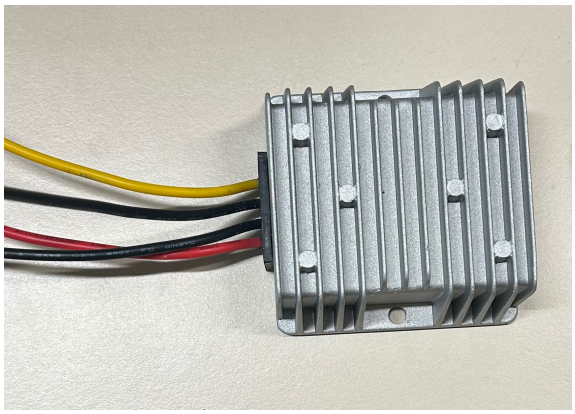

Figure 4.16: XW-24-12-120W model from XWST DC-DC converter.

4.1.6 Mini PC

The test bench is controlled by two NiPoGi AK1 Plus mini-PCs 4.17. These devices are characterized by compact dimensions ($132 \times 132 \times 52$ mm^3), well suited for this experiment, offering an excellent balance between portability and performance. The two mini-PCs are assigned different tasks: one manages the video acquisition from the monitoring cameras through Python scripts and an ESP32 microcontroller that

manages the trigger signals, while the other handles the acquisition of the markers on the proof mass via LabVIEW, being directly connected to the National Instruments data acquisition board.

Figure 4.17: NiPoGi AK1 Plus mini-PCs.

4.1.7 NI USB-6501 National Instrument Board

For monitoring the displacement markers on the proof mass, a National Instruments NI-USB-6501 data acquisition board was employed. This board provides a USB digital input-output interface with 24 TTL-compatible digital lines, supporting logic levels of 0–0.8 V (LOW) and 2–5 V (HIGH). It is powered directly via a USB 2.0 connection to the mini-PC and allows digital I/O operations with maximum update rates up to 5 MHz under hardware-timed configurations. In this setup 4.18, the board is connected to the wiring required for data acquisition, the powering of the LEDs, and the management of trigger signals.

Figure 4.18: NI USB-6501 National instrument board.

4.2 Displacement Acquisition Principle

In this section, the program developed for acquiring the displacement positions of the markers within the proof mass is presented. The software used is *LabVIEW*, a graphical programming environment widely employed in engineering applications for measurement and control automation. The program consists of two main components: the *Front Panel*, which serves as the human–machine interface and allows the user to interact intuitively with the application, and the *Block Diagram*, which defines the program logic through a dataflow-based graphical structure.

In this thesis, a detailed description of the *Front Panel* is provided, as it is essential for understanding the functioning of the experiment, while the *Block Diagram* is described in a more qualitative manner.

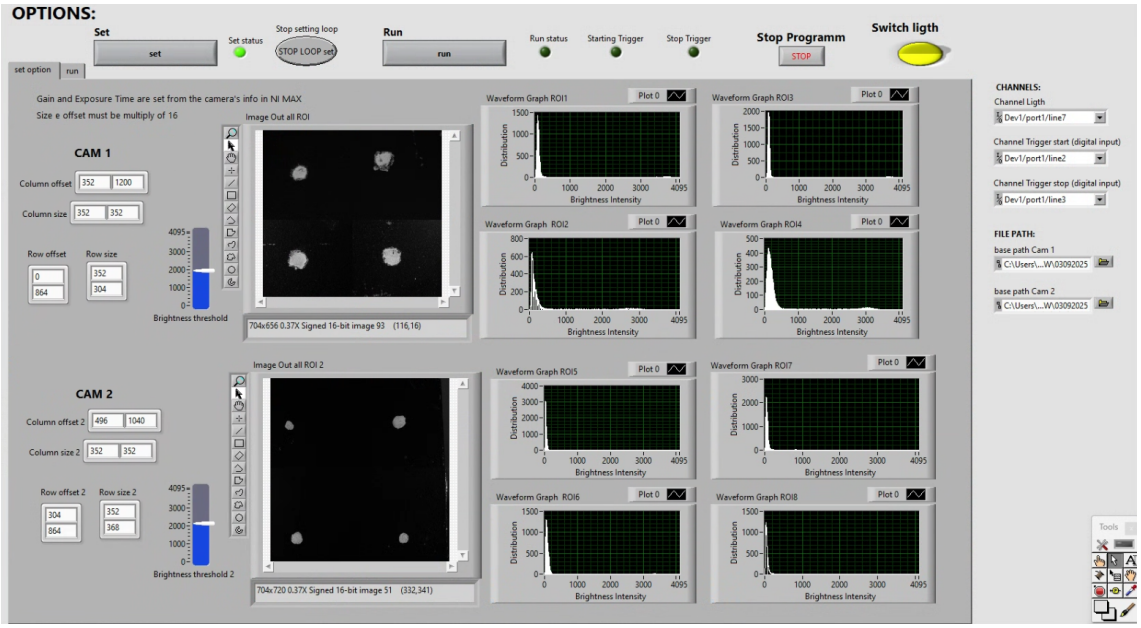

Figure 4.19: Setup Front Panel.

The program is divided into two phases: the setup and the running, both of which can be activated through switches. In the setup phase of the front panel (Figure 4.19), it is possible to modify the experiment configuration, namely the position of the mass, the position of the cameras, the zoom, and the offset that must be set

to ensure that the marker is centered in the image, while observing in real time the changes through the dedicated display. In addition, it is possible to check the operation of the LEDs through a specific button and to view the distribution of the brightness intensity of the image. The block diagram, instead, is organized through a sequence of operations that handle the video acquisition of the mass by means of a while loop, which can be exited by pressing the stop setting loop button.

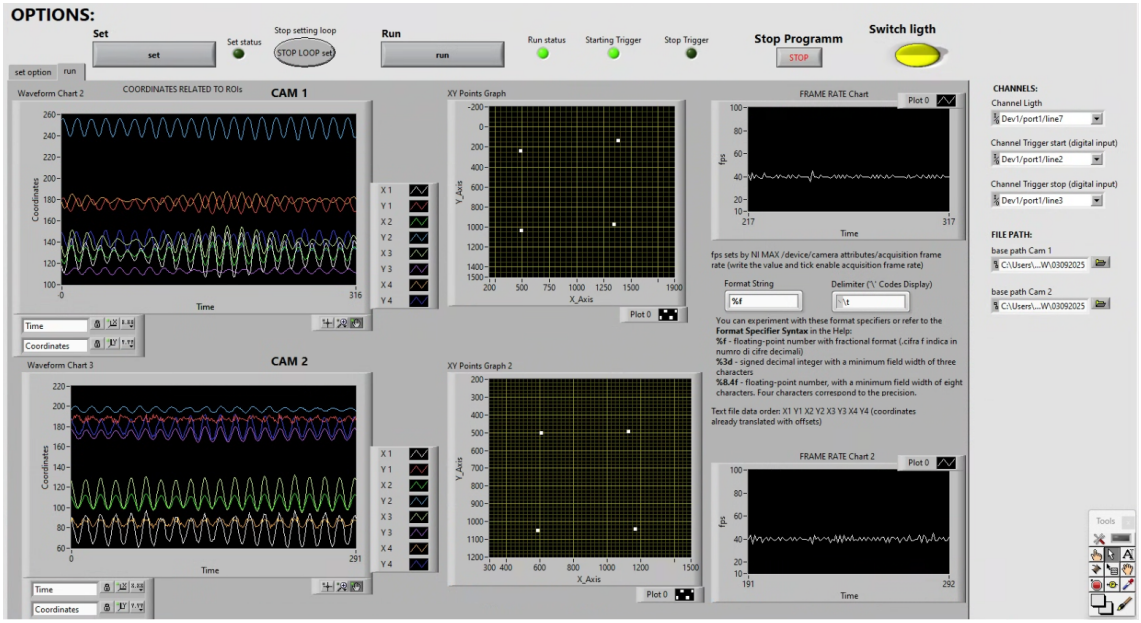

Figure 4.20: Running Front Panel.

In the running phase, the front panel (Figure 4.20) displays a graph showing the displacements of the centroid of the markers in the mass for each coordinate x and y. In addition, an x–y plot of the markers is presented, providing another method to visualize their position, while on the right side the frame rate chart for both cameras is shown, indicating the frames per second of each camera.

The block diagram, instead, is organized with an external while loop that allows the reception of start and stop acquisition triggers multiple times, until the program stop button is pressed. At the moment, these triggers are realized through physical switches, but they will later be replaced by signals from the Einstein Elevator, transmitting the start and stop launch triggers. As soon as the start trigger is

received, the program enters a structure in which the acquisition from both cameras takes place. The two acquisitions are managed by two independent loops where the centroid of the markers is calculated, in order to display their displacement on the front panel. When the stop trigger is received, the data are saved in text files named after the start of the launch, in order to keep track of the experimental runs.

4.3 Video Acquisition Principle for Experiment Monitoring

For the monitoring of the experiment, a Python script was developed to control the video acquisition, together with an ESP32 microcontroller dedicated to managing the triggers generated by the Einstein Elevator. Specifically, the microcontroller monitors dedicated input pins through interrupt service routines, detecting whether a trigger signal (`START`, `STOP`, or `ARM`) has been activated by evaluating its high or low logic level. As soon as a trigger is received, the ESP32 communicates the corresponding command via the serial port at a transmission rate of 115,200 baud.

The Python script runs on a mini-PC and manages two webcams, enabling synchronized recording triggered by the serial commands. The cameras are initialized at a resolution of 640×480 pixels with a frame rate of 60 fps. When a `START` trigger is detected, the recording begins, and when a `STOP` trigger is received, the acquisition ends. At that point, a video file in `.avi` format is automatically created for each camera, with filenames including a timestamp for traceability.

These videos serve both as a quantitative measure of the displacement of the markers and as a visual validation of the experiment. In addition, in the event of anomalies or malfunctions in the marker displacement acquisition system, the recorded videos provide a reliable backup to calculate the motion of the proof mass.

Figure 4.21 shows the ESP32 microcontroller setup used for trigger management, where the signals are simulated through push buttons.

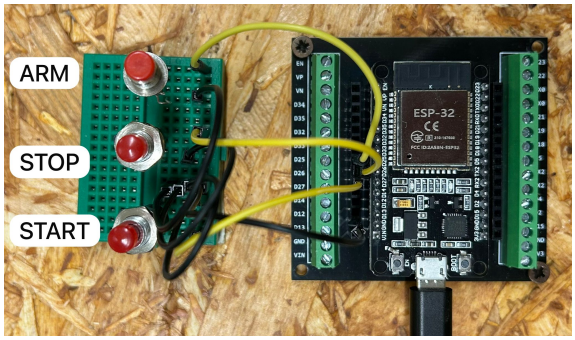

Figure 4.21: ESP32 microcontroller setup for trigger signal management.

Conclusions

In this thesis, a new accelerometer architecture based on a mass–spring system—with acceleration measurements derived from the heterodyne laser interferometric principle—was developed and analyzed. This technology is known for its high sensitivity and low noise, making it a competitive choice for space applications, such as *GRACE-FO* and *LISA Pathfinder*.

Because both acceleration sensitivity and noise scale with the square of the natural frequency, it was necessary to target the lowest possible natural frequency, set at 1 Hz. To meet this requirement, a spring was designed and manufactured via AM, specifically using PBF–LB. The approach involved a feasibility study, a process parameter investigation, and the fabrication of simplified springs, followed by the production of the final prototype, whose static and dynamic responses were characterized and compared against finite element simulations.

Additionally, a dedicated test bench was developed for the qualification of the accelerometer under microgravity conditions in the *Einstein Elevator* drop tower at HITec. The bench enables the measurement of the test mass displacement along all six degrees of freedom using an optical tracking system based on cameras, and it integrates auxiliary sensors to validate the experimental conditions.

In summary, the results demonstrate that the spring can be produced by AM; although some distortions were observed in the prototype, two bending natural frequencies were measured at 4.34 Hz and 4.50 Hz—sufficiently low to meet the required specification once the mass is added reaching approximately 0.46 Hz—and the axial stiffness was 0.0254 ± 0.0002 N/mm. Moreover, the FE model reproduces the physical behavior with errors below 8% for the bending natural frequencies. The test bench was also successfully validated, reliably acquiring marker displacements

and videos, handling triggers, and synchronizing auxiliary sensors for automated, streamlined operation.

Following this study, the next steps are: (i) to optimize the spring supports to eliminate residual distortions in the coils; (ii) to proceed with qualification in microgravity; and (iii) to initiate the *LIG-A CUBE MISSION*. The goal is to qualify the complete system—accelerometer and interferometer—and to assess the feasibility of scaling this accelerometer concept toward industrial production.

Appendix

4.4 Description of Einstein Elevator [12] [25]

The Einstein Elevator is an active drop tower located at the Hannover Institute of Technology of the Leibniz University of Hannover. An active drop tower is a facility that enables the simulation of different microgravity conditions through a motorized system. Figure 4.22 illustrates the design of the Einstein Elevator in detail.

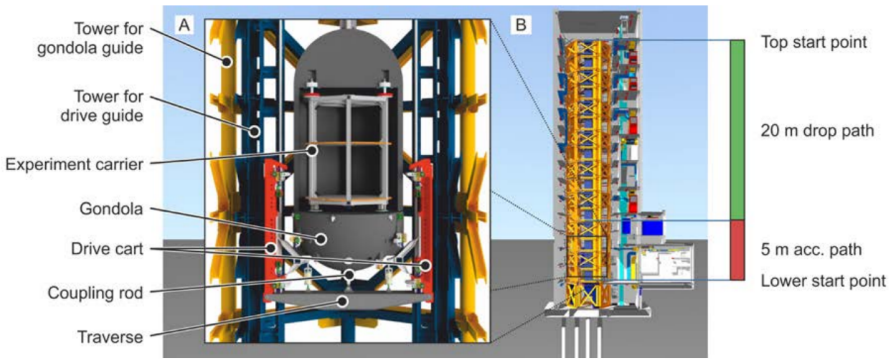

Figure 4.22: Design of the Einstein Elevator [12].

Figure A illustrates a cross-section of the steel structure together with the gondola containing an empty experiment carrier, whereas Figure B presents a schematic representation of the tower highlighting its different functional zones.

Thanks to its motorized system, the facility can perform microgravity experiments not only by releasing the gondola from the top of the tower but also by launching it upwards from the bottom, thus creating a parabolic trajectory that extends the effective microgravity duration. The gondola's driving section measures 27 m, with 20 m available for free fall. This configuration allows test durations of up to 4 s, depending on the simulated gravity level, with a high repetition rate of up to 300 tests per day and rapid modifications between successive launches.

The tower can accommodate payloads up to 1000 kg, with a maximum experimental volume of 1.7 m in diameter and 2 m in height, while ensuring a residual acceleration below $10^{-6}g$. Figures 4.23 and 4.24 present, respectively, the acceleration curves obtained for different driving profiles and the experiment duration as a function of the simulated gravity conditions.

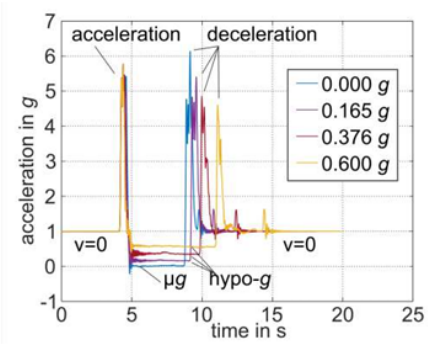

Figure 4.23: Acceleration curves of selected driving profiles [25].

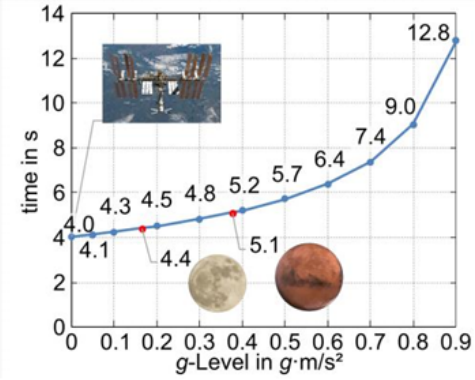

Figure 4.24: Experiment duration under different gravity conditions [25].

In Figure 4.25, the Position–Speed diagrams for microgravity and hypogravity experiments are presented, showing the velocity reached by the gondola at different heights of the drop tower. Figure A illustrates the parabolic launch configuration, while Figure B shows the pure free-fall case.

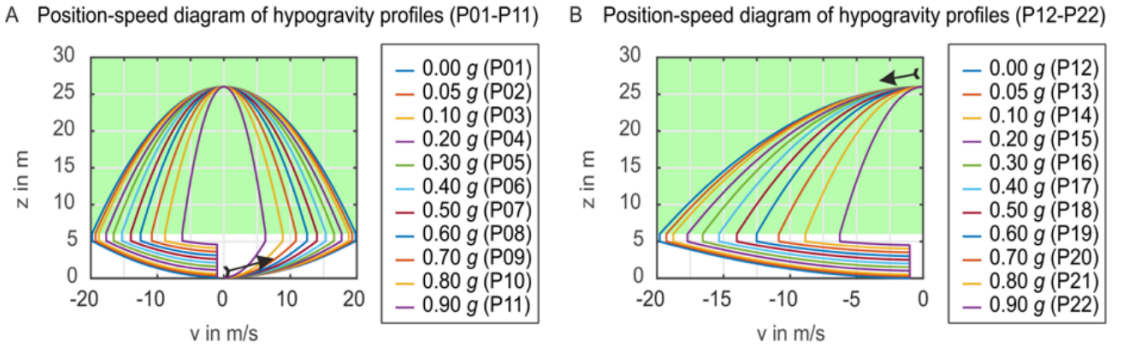

Figure 4.25: Position–Speed diagrams for micro- and hypogravity experiments [12].

The experiments can be carried out under two different configurations (Figure 4.26): either in vacuum or in an inert gas atmosphere using a dedicated chamber (Figure A), or at ambient pressure (Figure C). In addition, the experiment carrier can be adapted to different loading conditions by integrating modular platforms and structural elements that can be assembled or removed to increase stiffness if required.

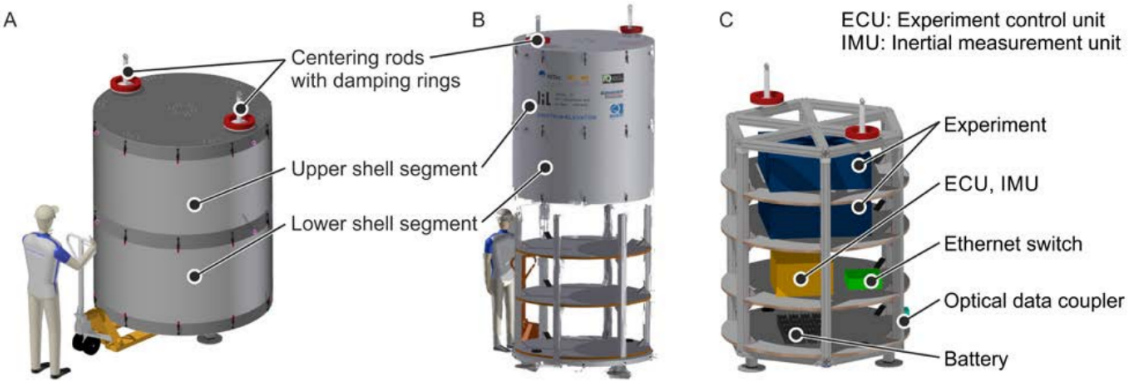

Figure 4.26: Configurations of the experiment carrier [12].

The carrier is also equipped with dedicated cameras for video monitoring and experiment observation, together with sensors measuring acceleration,position, rotation, temperature, pressure and humidity. Regarding the electrical interface, it features an FGG.2B.302.CYCD82 connector for a 24 V DC power supply, as shown in Figure 4.27, and an FGG.2B.316.CYCD82 connector that provides status and

trigger signals at either 3.3 or 5 V DC, illustrated in Figure 4.28. In addition, wireless connectivity (Wi-Fi) and Fast Ethernet via an 8-pin connector are available.

24 V DC internal power supply	FGG.2B.302.CYCD82 	1	24 V DC	Fused with 16 A
		2	GND	

Figure 4.27: FGG.2B.302.CYCD82 connector for power supply [25].

Status and trigger signals	FGG.2B.316.CYCD82 	1	DO1, Launch	3,3 V DC/5 V DC, 20 mA
		2	DO2, End of Flight	3,3 V DC/5 V DC, 20 mA
		3	DO3, Pre Launch Trigger	3,3 V DC/5 V DC, 20 mA
		4	DO4, Start µg phase	3,3 V DC/5 V DC, 20 mA
		5	DO5, Abort (Pre Launch)	3,3 V DC/5 V DC, 20 mA
		6	DO6, Emergency stop (Launch)	3,3 V DC/5 V DC, 20 mA
		7	DO7, configurable	3,3 V DC/5 V DC, 20 mA
		8	DO8, configurable	3,3 V DC/5 V DC, 20 mA
		9	GND	Common ground for pin 1-8

Figure 4.28: FGG.2B.316.CYCD82 connector for status and trigger signals [25].

Bibliography

[1] S. Ciuffreda. "Design of the elastic suspension for a new concept accelerometer for space applications: LIG-A-CUBE mission". PhD thesis. Politecnico di Torino, 2023.

[2] M. Pisani and M. Zucco. *LIG-A: Laser Interferometry Gauge & Accelerometer*. ESA Proposal AO/1-8876/17/NL/CRS, ITI type B, Proposal No. 1000019244-8000014585-1, ESA CN 4000125653. European Space Agency, 2021.

[3] V. Iafolla, E. Fiorenza, C. Lefevre, et al. "The ISA accelerometer for Bepi-Colombo mission". In: *Memorie della Società Astronomica Italiana Supplement* 16 (2011), p. 22.

[4] F. Santoli, E. Fiorenza, C. Lefevre, et al. "ISA, a High Sensitivity Accelerometer in the Interplanetary Space: Updates after the Near-Earth Commissioning Phase of Italian Spring Accelerometer–ISA". In: *Space Science Reviews* 216.8 (2020), p. 145.

[5] J. Benkhoff, G. Murakami, W. Baumjohann, et al. "BepiColombo—mission overview and science goals". In: *Space Science Reviews* 217.8 (2021), p. 90.

[6] M. Pisani and M. Zucco. "An accelerometer for spaceborne application with interferometric readout". In: *Measurement* 122 (2018), pp. 507–512.

[7] D. I. Robertson, E. D. Fitzsimons, C. J. Killow, et al. "Construction and testing of the optical bench for LISA Pathfinder". In: *Classical and Quantum Gravity* 30.8 (2013), p. 085006.

[8] G. Heinzel, B. Sheard, N. Brause, et al. "Laser ranging interferometer for GRACE-FO". In: *International Conference on Space Optics—ICSO 2012*. Vol. 10564. SPIE. 2017, pp. 517–526.

[9] A. M. Nobili, M. Pisani, and M. Zucco. *LIG: a miniature 10 pm accuracy Laser Interferometer Gauge. Report of work performed under ESA contract ITI 4000116275/16/NL/MH/GM*. Technical Report. European Space Agency, 2016.

[10] M. Pisani. *LIG-A CUBE Requirements Review*. Internal Report. INRiM / ESA, 2023.

[11] M. Hoffmann Rodriguez and A. Elwany. "In-Space Additive Manufacturing: A Review". In: *Journal of Manufacturing Science and Engineering* 145 (Sept. 2022), pp. 1–70. DOI: 10.1115/1.4055603.

[12] C. Lotz, T. Froböse, A. Wanner, L. Overmeyer, and W. Ertmer. "Einstein-Elevator: A New Facility for Research from μg to 5 g". In: *Gravitational & Space Research* 5.2 (2017).

[13] UP Aerospace. *Spaceloft XL*. 2015. URL: https://www.celestis.com/blog/launch-vehicle-spotlight-up-aerospace-s-spaceloft-xl/.

[14] Thomas Pesquet, ESA. *ISS*. 2021. URL: https://www.flickr.com/photos/nasa2explore/albums/72157720187084178/.

[15] Mondial S.p.A. *HELI-CAL*. 2025. URL: https://www.mondial.it/euronet/contenuti/image/thumb/helical.pdf.

[16] Fraunhofer IFAM. *Description of the Laser Beam Melting process*. 2023. URL: https://www.ifam.fraunhofer.de/en/technologies/laser-beam-melting.html.

[17] EOS GmbH. *EOS Titanium Ti64 Grade 5 — Material Data Sheet*. 2019. URL: https://www.eos.info/03_system-related-assets/material-related-contents/metal-materials-and-examples/metal-material-datasheet/titan/ti64/material_datasheet_eos_titanium_ti64_grade5_en_web.pdf.

[18] EOS GmbH. *EOS Aluminium AlSi10Mg — Material Data Sheet*. 2025. URL: https://www.eos.info/metal-solutions/metal-materials/data-sheets/mds-eos-aluminium-alsi10mg?pdf=1&topdf=%2Fmetal-solutions%2Fmetal-materials%2Fdata-sheets%2Fmds-eos-aluminium-alsi10mg.

[19] EOS GmbH. *EOS NickelAlloy IN718 — Material Data Sheet*. 2024. URL: https://www.eos.info/05-datasheet-images/Assets_MDS_Metal/EOS_NickelAlloy_IN718/Material_DataSheet_EOS_NickelAlloy_IN718_en.pdf.

[20] EOS GmbH. *EOS StainlessSteel 316L — Material Data Sheet*. 2022. URL: https://www.eos.info/03_system-related-assets/material-related-contents/metal-materials-and-examples/metal-material-datasheet/stainlesssteel/material_datasheet_eos_stainlesssteel_316l_en_web.pdf.

[21] Advanced Powders and Coatings. *Ti-6Al-4V Grade 23 Specifics*. 2025. URL: https://www.advancedpowders.com/powders/titanium-alloys-ti-6al-4v-grade-23.

[22] S. Tammas-Williams, P. J. Withers, I. Todd, and P. B. Prangnell. "Porosity regrowth during heat treatment of hot isostatically pressed additively manufactured titanium components". In: *Scripta Materialia* 122 (2016), pp. 72–76. DOI: 10.1016/j.scriptamat.2016.05.002.

[23] B. Meier, N. Godja, F. Warchomicka, et al. "Influences of Surface, Heat Treatment, and Print Orientation on the Anisotropy of the Mechanical Properties and the Impact Strength of Ti-6Al-4V Processed by Laser Powder Bed Fusion". In: *Journal of Manufacturing and Materials Processing* 6.4 (2022), p. 87. DOI: 10.3390/jmmp6040087.

[24] M. Zhang et al. "Ti–6Al–4V alloy prepared by laser powder bed fusion: post-processing under vacuum". In: *Materials Research Letters* (2024). DOI: 10.

1080/25787616.2024.2315716. URL: https://www.tandfonline.com/doi/full/10.1080/25787616.2024.2315716.

[25] HITec. *Einstein Elevator technical guide*. URL: https://www.uni-hannover.de/en/.